Draft version February 4, 2013
Preprint typeset using LaTeX style emulateapj v. 11/10/09

PS1-10afx at $z = 1.388$: Pan-STARRS1 Discovery of a New Type of Superluminous Supernova

R. Chornock[1], E. Berger[1], A. Rest[2], D. Milisavljevic[1], R. Lunnan[1], R. J. Foley[1,3], A. M. Soderberg[1], S. J. Smartt[4], A. J. Burgasser[5], P. Challis[1], L. Chomiuk[6], I. Czekala[1], M. Drout[1], W. Fong[1], M. E. Huber[7], R. P. Kirshner[1], C. Leibler[8], B. McLeod[1], G. H. Marion[1], G. Narayan[1], A. G. Riess[2,9], K. C. Roth[10], N. E. Sanders[1], D. Scolnic[9], K. Smith[3], C. W. Stubbs[1,11], J. L. Tonry[7], S. Valenti[12], W. S. Burgett[7], K. C. Chambers[7], K. W. Hodapp[7], N. Kaiser[7], R.-P. Kudritzki[7], and P. A. Price[13]

Draft version February 4, 2013

ABSTRACT

We present the Pan-STARRS1 discovery of PS1-10afx, a unique hydrogen-deficient superluminous supernova (SLSN) at redshift $z = 1.388$. The light curve peaked at $z_{\rm P1} = 21.7$ mag, making PS1-10afx comparable to the most luminous known SNe, with $M_u = -22.3$ mag. Our extensive optical and near-infrared observations indicate that the bolometric light curve of PS1-10afx rose on the unusually fast timescale of $\sim$12 d to the extraordinary peak luminosity of 4.1×10^{44} erg s^{-1} ($M_{\rm bol} = -22.8$ mag) and subsequently faded rapidly. Equally important, the SED is unusually red for a SLSN, with a color temperature of $\sim$6800 K near maximum light, in contrast to previous hydrogen-poor SLSNe, which are bright in the ultraviolet (UV). The spectra more closely resemble those of a normal SN Ic than any known SLSN, with a photospheric velocity of $\sim$11,000 km s^{-1} and evidence for line blanketing in the rest-frame UV. Despite the fast rise, these parameters imply a very large emitting radius ($\gtrsim5\times10^{15}$ cm). We demonstrate that no existing theoretical model can satisfactorily explain this combination of properties: (i) a nickel-powered light curve cannot match the combination of high peak luminosity with the fast timescale; (ii) models powered by the spindown energy of a rapidly-rotating magnetar predict significantly hotter and faster ejecta; and (iii) models invoking shock breakout through a dense circumstellar medium cannot explain the observed spectra or color evolution. The host galaxy is well detected in pre-explosion imaging with a luminosity near L^*, a star formation rate of $\sim$15 M$_\odot$yr^{-1}, and is fairly massive ($\sim2\times10^{10}$ M$_\odot$), with a stellar population age of $\sim10^8$ yr, also in contrast to the young dwarf hosts of known hydrogen-poor SLSNe. PS1-10afx is distinct from known examples of SLSNe in its spectra, colors, light-curve shape, and host galaxy properties, suggesting that it resulted from a different channel than other hydrogen-poor SLSNe.

Subject headings: supernovae: individual (PS1-10afx)

1. INTRODUCTION

A small fraction of massive stars end their lives with spectacular explosions one or two orders of magnitude more luminous than normal supernovae (SNe). After the initial puzzling discoveries of the luminous SNe 2005ap (Quimby et al. 2007) and 2006gy (Ofek et al. 2007; Smith et al. 2007), modern wide-field surveys over the past decade began to uncover these superluminous SNe (SLSNe) in greater numbers. The energy scales involved in these explosions challenge our understanding of conventional SN explosions. Normal SNe resulting from iron core collapse have characteristic energy scales of $\sim10^{51}$ erg of kinetic energy and $\sim10^{49}$ erg emitted as optical radiation ($\sim10^{42}$ erg s^{-1} for $\sim10^7$ s). The SLSNe are far off this scale— they peak at optical luminosities of up to $\sim4\times10^{44}$ erg s^{-1} (Quimby et al. 2011; Chomiuk et al. 2011; Miller et al. 2009; Gezari et al. 2009) and emit a total of up to 4×10^{51} erg optically (Rest et al. 2011).

This large energy scale motivates the question of what physics powers these SNe, and how to accommodate these objects within the standard understanding of massive star evolution. Theorists have proposed a number of exotic power sources, including the pair instability mechanism (e.g., Barkat et al. 1967; Rakavy & Shaviv 1967) and reprocessed spindown energy released by a newly formed magnetar (Woosley 2010; Kasen & Bildsten 2010). Another possibility is interaction with a dense circumstellar medium (CSM) (Chevalier & Irwin 2011; Moriya & Tominaga 2012; Ginzburg & Balberg 2012; Chatzopoulos et al. 2012), requiring extreme CSM masses and densities whose origin remains unexplained (see Woosley et al. 2007 for one possibility). All of these

[1] Harvard-Smithsonian Center for Astrophysics, 60 Garden St., Cambridge, MA 02138, USA, rchornock@cfa.harvard.edu
[2] Space Telescope Science Institute, 3700 San Martin Drive, Baltimore, MD 21218, USA
[3] Clay Fellow
[4] Astrophysics Research Centre, School of Mathematics and Physics, Queen's University Belfast, Belfast, BT7 1NN, UK
[5] Center for Astrophysics and Space Science, University of California San Diego, La Jolla, CA 92093, USA
[6] Jansky Fellow; Department of Physics and Astronomy, Michigan State University, East Lansing, MI 48824, USA
[7] Institute for Astronomy, University of Hawaii, 2680 Woodlawn Drive, Honolulu HI 96822, USA
[8] Department of Astronomy & Astrophysics, University of California, Santa Cruz, CA 95060, USA
[9] Department of Physics and Astronomy, Johns Hopkins University, 3400 North Charles Street, Baltimore, MD 21218, USA
[10] Gemini Observatory, 670 North Aohoku Place, Hilo, HI 96720, USA
[11] Department of Physics, Harvard University, 17 Oxford Street, Cambridge, MA 02138, USA
[12] Las Cumbres Observatory Global Telescope Network, Inc., Santa Barbara, CA 93117, USA; Department of Physics, University of California Santa Barbara, Santa Barbara, CA 93106-9530, USA
[13] Department of Astrophysical Sciences, Princeton University, Princeton, NJ 08544, USA

models require additional ingredients beyond the normal stellar evolutionary processes.

Gal-Yam (2012) has attempted to impose order on the menagerie of objects achieving sufficient peak luminosities to be classified as SLSNe ($M < -21$ mag is a typical requirement) by sorting them into three categories. All of the hydrogen-rich objects were classified as SLSNe-II and all exhibit signs of being powered by dense CSM interaction, with the possible exception of SN 2008es (Miller et al. 2009; Gezari et al. 2009). He split the objects lacking hydrogen into two classes, the rare SLSNe-R that have slow photometric decline rates consistent with being powered by the radioactive decay of a very large synthesized mass of ^{56}Ni, and the relatively homogeneous class of SLSNe-I, whose power source is still mysterious. A few caveats have been raised. The SLSNe-R are interpreted to be the results of pair-instability SNe. However, existing models for the pair instability process prefer extremely low metallicity, and may be in conflict with the observed spectrum and spectral energy distribution (SED) of SLSNe-R (e.g., Dessart et al. 2012b). Also, it is not clear how homogeneous the SLSNe-I class really is. Although the spectra of most appear to be similar to those of SN 2005ap and SCP06F6 (Quimby et al. 2007; Barbary et al. 2009), the rise times and peak luminosities of published objects vary by factors of $\sim$5 (Quimby et al. 2007; Pastorello et al. 2010; Quimby et al. 2011; Chomiuk et al. 2011; Leloudas et al. 2012; Lunnan et al. 2013). All SLSNe-I to date have had hot spectra and been bright in the rest-frame near-ultraviolet (NUV) relative to normal SN SEDs.

In this paper, we present the discovery of PS1-10afx, an extreme SLSN at redshift $z = 1.388$ that does not fit into this classification scheme and is distinct from all previous SLSNe. The peak luminosity is comparable to the highest known and the rise time is the fastest measured. The spectra show no evidence for hydrogen and lack any analog in the existing sample of SLSNe. Instead, they most closely resemble those of line-blanketed normal SNe Ic. In Section 2, we present the suite of optical and near-infrared (NIR) observations. The host galaxy is described in Section 3. We compare our observations of PS1-10afx to known SNe in Section 4. In Section 5, we construct the SED and bolometric light curve. We then compare PS1-10afx to existing SLSN models in Section 6. All calculations in this paper assume a flat ΛCDM cosmology with H_0=74 km s^{-1} Mpc^{-1}, Ω_m=0.27, and Ω_Λ=0.73 (Komatsu et al. 2011; Riess et al. 2011).

2. OBSERVATIONS

2.1. *Pan-STARRS1*

The Pan-STARRS1 (PS1) telescope has a 1.8 m diameter primary mirror that images a field with a diameter of 3.3°(Hodapp et al. 2004) onto a total of sixty 4800 × 4800 pixel detectors, with a pixel scale of 0.258″(Tonry & Onaka 2009). A more complete description of the PS1 system, hardware and software, is provided by Kaiser et al. (2010).

The PS1 observations are obtained through a set of five broadband filters, designated as $g_{\rm P1}$, $r_{\rm P1}$, $i_{\rm P1}$, $z_{\rm P1}$, and $y_{\rm P1}$. Although the filter system for PS1 has much in common with that used in previous surveys, such as the Sloan Digital Sky Survey (SDSS; Ahn et al. 2012), there are differences. Most important for this work, the $z_{\rm P1}$ filter is cut off at 9300 Å, giving it a different response than the detector response defined z_{SDSS}, and SDSS has no corresponding $y_{\rm P1}$ filter. Further information on the passband shapes is described by Stubbs et al. (2010). Photometry is in the "natural" PS1 system, $m = -2.5\log(f_\nu) + m'$, with a single zeropoint adjustment m' made in each band to conform to the AB magnitude scale (Tonry et al. 2012). Photometry from all other sources presented in this paper is also on the AB scale. PS1 magnitudes are interpreted as being at the top of the atmosphere, with 1.2 airmasses of atmospheric attenuation being included in the system response function.

The PS1 Medium Deep Survey (MDS) consists of 10 fields across the sky that are observed nightly when in season ($\sim$5 months per year) with a typical cadence of 3 d between observations in $g_{\rm P1}r_{\rm P1}i_{\rm P1}z_{\rm P1}$ in dark and gray time, while $y_{\rm P1}$ is used near full moon. PS1 data are processed through the Image Processing Pipeline (IPP; Magnier 2006) on a computer cluster at the Maui High Performance Computer Center. The pipeline runs the images through a succession of stages, including flat-fielding ("de-trending"), a flux-conserving warping to a sky-based image plane, masking and artifact removal, and object detection and photometry. Transient detection using IPP photometry is carried out at Queens University Belfast. Independently, difference images are produced from the stacked nightly MDS images by the `photpipe` pipeline (Rest et al. 2005) running on the Odyssey computer cluster at Harvard University. The discovery and data presented here are from the `photpipe` analysis.

PS1-10afx was first detected in MDS imaging on 2010 August 31.35 (UT dates are used throughout this paper) at a position of $\alpha = 22^{\rm h}11^{\rm m}24\overset{\rm s}{.}162$, $\delta = +00°09'43\overset{''}{.}49$ (J2000), with an uncertainty of $0\overset{''}{.}1$ in each coordinate. The strong detections in $i_{\rm P1}$ and $z_{\rm P1}$ combined with non-detections in $g_{\rm P1}$ and $r_{\rm P1}$ over the next few nights immediately garnered our attention. The unusual colors are evident in the color images of the field presented in Figure 1.

We constructed deep template stacks from all pre-explosion images and subtracted them from the PS1 observations using `photpipe` (Rest et al. 2005). Details of the photometry and generation of PS1 SN light curves will be given by Rest et al. (2013, in prep.) and Scolnic et al. (2013, in prep.). The typical spacing between MDS observations in the same filter corresponds to only 1.3 d in the rest frame of PS1-10afx, so in some cases we have co-added the photometry from adjacent observations to increase the significance of marginal detections or the depth of the non-detections. The final PS1-10afx photometry, after correction for $E(B-V) = 0.05$ mag of Galactic extinction (Schlafly & Finkbeiner 2011; Schlegel et al. 1998), is given in Table 1 and shown in Figure 2.

We fit polynomials to the $z_{\rm P1}$ data points within 15 rest-frame days of peak to determine the time of maximum light, for which we adopt a Modified Julian Date (MJD) of 55457.0 (=2010 September 18.0). All phases referred to subsequently are in rest-frame days referenced from this date.

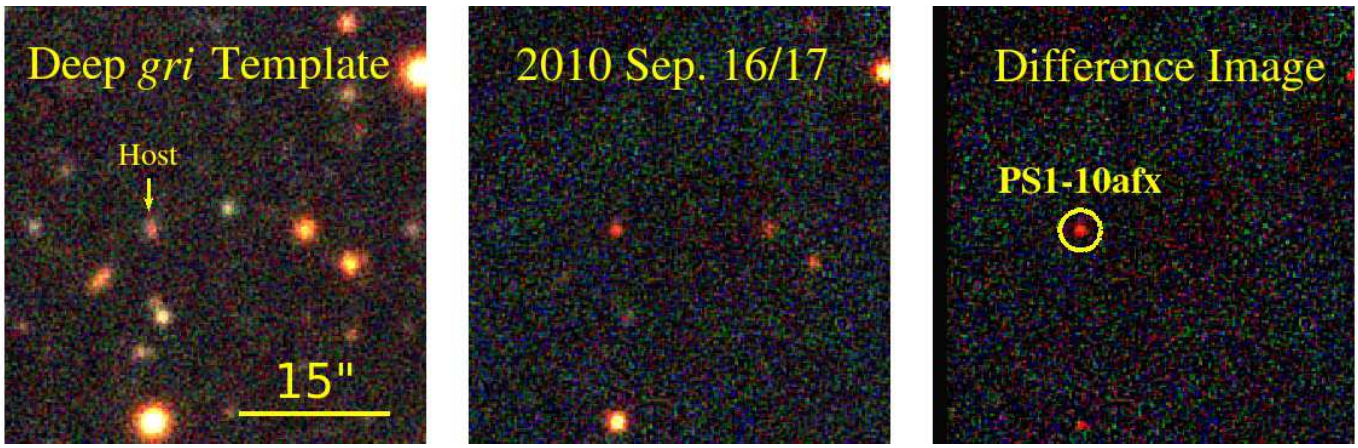

Figure 1. Three-color $g_{P1}r_{P1}i_{P1}$ images of the field of PS1-10afx, showing (*left*) a deep stack of pre-explosion imaging with the host galaxy marked; (*center*) images taken near maximum light; and (*right*) difference images of the templates subtracted from the observations. The color scales are similar in each panel. The unusually red color of PS1-10afx compared to other faint objects in the field is apparent, as it is only strongly detected in i_{P1}, with non-detections in g_{P1} and r_{P1}.

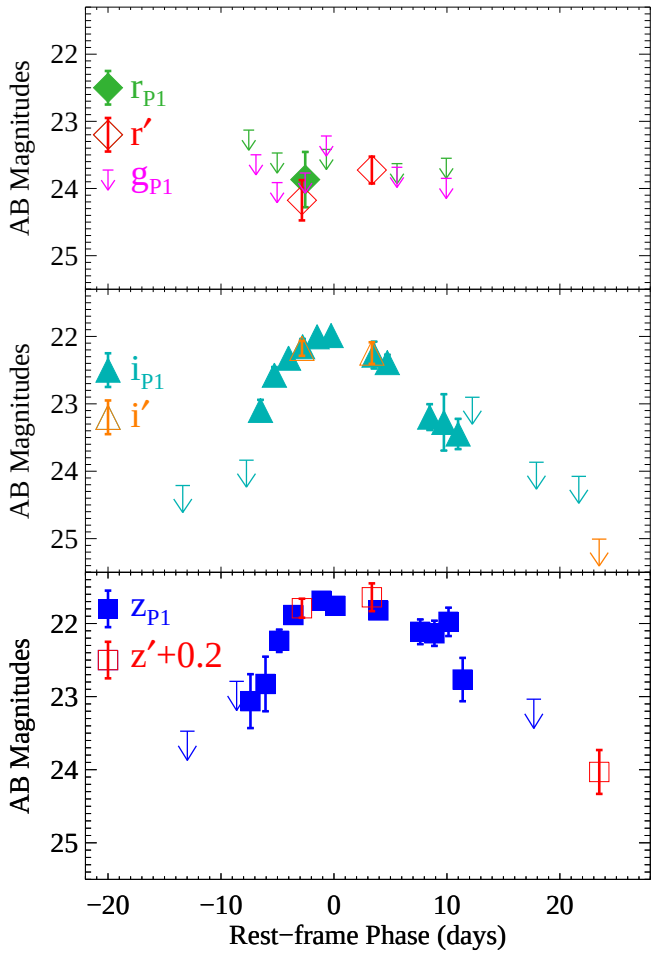

Figure 2. Multicolor optical light curves of PS1-10afx. Most of the data were obtained with PS1, but points marked r', i', or z' come from other telescopes (see Table 1). The $r'i'z'$ photometry points near days −3 and +3 were taken contemporaneously with the optical spectra shown in Figure 3. Upper limits marked with arrows correspond to 3σ.

2.2. *Other Optical Photometry*

In addition to the PS1 observations, we obtained two epochs of multicolor photometry using the Gemini Multi-Object Spectrographs (GMOS; Hook et al. 2004) on the 8-m Gemini-North and South telescopes and one epoch of imaging using the Inamori-Magellan Areal Camera and Spectrograph (IMACS; Dressler et al. 2006) on the 6.5-m Magellan Baade telescope. The images were processed using standard tasks and then archival fringe frames were subtracted from the GMOS images using the `gemini` IRAF[14] package. We used several SDSS stars in the field to calibrate the Gemini images, while the IMACS zeropoints were checked with observations of standard star fields obtained the same night. We subtracted the deep PS1 templates in the corresponding filter from each image using the ISIS software package (Alard & Lupton 1998) to correct for host contamination. The final photometry is listed in Table 1. The r' and i' magnitudes agree well with the PS1 observations at similar epochs. However, the z' observations exhibit an offset from the z_{P1} light curve due to the filter response differences noted above (GMOS and IMACS are closer to SDSS). We therefore add 0.2 mag to the z' photometry points for consistency with z_{P1} whenever we refer to the combined z-band light curve. Finally, we obtained late-time observations of the host galaxy in g' and r' on 2011 October 21.1 using the Low Dispersion Survey Spectrograph-3 (LDSS3) on the 6.5-m Magellan Clay telescope.

2.3. *Optical Spectroscopy*

After noticing the unusually red $r_{P1}-i_{P1}$ colors of PS1-10afx, we immediately triggered optical spectroscopy using GMOS-N. A pair of dithered 1800 s observations were taken on 2010 September 11.26 (phase −2.8 d) with the R400 grating and OG515 order-blocking filter to cover the wavelength range of 5400−9650 Å. We used standard tasks in IRAF to perform basic two-dimensional image processing and spectral extraction. We used our

[14] IRAF is distributed by the National Optical Astronomy Observatories, which are operated by the Association of Universities for Research in Astronomy, Inc., under cooperative agreement with the National Science Foundation.

Table 1
PS1-10afx Photometry

MJD	Epoch[a] (d)	Filter	Magnitude[b] (AB)	Error	Instrument
55440.5[c]	−6.9	g_{P1}	>23.50	···	PS1
55445.0[c]	−5.0	g_{P1}	>23.91	···	PS1
55450.9[c]	−2.6	g_{P1}	>23.77	···	PS1
55455.4[c]	−0.7	g_{P1}	>23.22	···	PS1
55470.3[c]	5.6	g_{P1}	>23.68	···	PS1
55480.7[c]	9.9	g_{P1}	>23.85	···	PS1
55439.0[c]	−7.5	r_{P1}	>23.13	···	PS1
55445.0[c]	−5.0	r_{P1}	>23.47	···	PS1
55450.2	−2.8	r'	24.18	0.30	GMOS-N
55450.9[c]	−2.5	r_{P1}	23.87	0.41	PS1
55455.4[c]	−0.7	r_{P1}	>23.42	···	PS1
55465.0	3.4	r'	23.73	0.20	GMOS-S
55470.3[c]	5.6	r_{P1}	>23.63	···	PS1
55480.8[c]	9.9	r_{P1}	>23.55	···	PS1
55425.0[c]	−13.4	i_{P1}	>24.21	···	PS1
55438.5[c]	−7.7	i_{P1}	>23.84	···	PS1
55441.5	−6.5	i_{P1}	23.10	0.16	PS1
55444.4	−5.3	i_{P1}	22.57	0.12	PS1
55447.4	−4.0	i_{P1}	22.32	0.06	PS1
55450.4	−2.8	i_{P1}	22.15	0.11	PS1
55450.2	−2.8	i'	22.18	0.11	GMOS-N
55453.4	−1.5	i_{P1}	22.00	0.05	PS1
55456.4	−0.3	i_{P1}	21.99	0.05	PS1
55465.0	3.4	i'	22.25	0.16	GMOS-S
55465.5	3.5	i_{P1}	22.28	0.20	PS1
55468.3	4.7	i_{P1}	22.39	0.12	PS1
55477.2	8.5	i_{P1}	23.20	0.19	PS1
55480.2	9.7	i_{P1}	23.28	0.42	PS1
55483.2	11.0	i_{P1}	23.45	0.22	PS1
55486.3	12.2	i_{P1}	>22.90	···	PS1
55499.8[c]	17.9	i_{P1}	>23.87	···	PS1
55508.8[c]	21.7	i_{P1}	>24.08	···	PS1
55513.1	23.5	i'	>25.01	···	IMACS
55426.0[c]	−13.0	z_{P1}	>23.47	···	PS1
55436.4	−8.6	z_{P1}	>22.79	···	PS1
55439.3	−7.4	z_{P1}	23.06	0.37	PS1
55442.5	−6.1	z_{P1}	22.83	0.37	PS1
55445.4	−4.8	z_{P1}	22.24	0.15	PS1
55448.4	−3.6	z_{P1}	21.88	0.12	PS1
55450.2	−2.8	z'	21.59	0.13	GMOS-N
55454.4	−1.1	z_{P1}	21.69	0.10	PS1
55457.3	0.1	z_{P1}	21.76	0.11	PS1
55465.0	3.4	z'	21.44	0.19	GMOS-S
55466.4	3.9	z_{P1}	21.82	0.10	PS1
55475.2	7.6	z_{P1}	22.11	0.17	PS1
55478.2	8.9	z_{P1}	22.13	0.17	PS1
55481.2	10.1	z_{P1}	21.98	0.19	PS1
55484.2	11.4	z_{P1}	22.77	0.30	PS1
55499.2[c]	17.7	z_{P1}	>23.04	···	PS1
55513.1	23.5	z'	23.83	0.30	IMACS
55463.4	2.7	y_{P1}	21.09	0.16	PS1
55492.8[c]	15.0	y_{P1}	>21.95	···	PS1
55523.3	27.8	y_{P1}	>21.82	···	PS1
55463.4	2.7	Y	20.96	0.10	NIRI
55463.3	2.6	J	20.99	0.17	MMIRS
55463.4	2.7	J	21.19	0.10	NIRI
55481.1	10.1	J	22.22	0.26	MMIRS
55485.0	11.7	J	22.28	0.30	MMIRS
55496.0	16.3	J	22.19	0.10	HAWK-I
55515.1	24.3	J	22.84	0.14	HAWK-I
55552.0	39.8	J	>21.90	···	HAWK-I
55561.0	43.6	J	>21.90	···	HAWK-I
55463.4	2.7	H	21.20	0.19	NIRI
55485.0	11.7	H	21.05	0.44	MMIRS
55490.1	13.9	H	21.94	0.24	HAWK-I
55515.1	24.3	H	22.28	0.39	HAWK-I
55463.4	2.7	K	21.46	0.26	NIRI
55485.0	11.7	K_s	>21.35	···	MMIRS

[a] In rest-frame days relative to maximum light on MJD 55457.0.
[b] Corrected for Galactic reddening. Upper limits are 3σ.
[c] Data point is from a stack of observations taken on multiple nights. MJD reported is mean of individual observations in stack.

own IDL procedures to apply a flux calibration and correct for telluric absorption based on archival observations of spectrophotometric standard stars. The observations were performed at a mean airmass of 1.5, but the 1″-wide long slit was oriented within 20° of the parallactic angle (Filippenko 1982), so the overall spectral shape is reliable at these red wavelengths.

A second epoch of spectroscopy was obtained on 2010 September 26.04 (phase +3.4 d) using GMOS-S. The observations and instrumental setup were similar to the first epoch, except that a redder grating tilt was used to cover the range 5880−10100 Å. This spectrum has a lower signal-to-noise ratio (S/N) than the first one, but the main SN features are still present. We attempted a final epoch of spectroscopy using GMOS-S in nod-and-shuffle mode on 2010 November 5, but PS1-10afx had faded significantly, so we only detected a faint continuum with a hint of SN features. We do not consider this spectrum further.

The two spectra are shown in Figure 3. All of our optical spectra exhibit an emission line near 8903 Å, which we identify as [O II] λ3727 emission from the host galaxy, as well as absorption from the Mg II λ2800 doublet at the same redshift of $z = 1.388$, which we adopt as the SN redshift.

2.4. *NIR Photometry*

The high redshift and red optical colors of PS1-10afx indicate that NIR photometry is required to constrain the SED and bolometric luminosity. We received director's discretionary (DD) time at Gemini-North to obtain $YJHK$ photometry near maximum light using the Near InfraRed Imager and Spectrometer (NIRI; Hodapp et al. 2003). The observations were acquired on 2010 September 24.4, at a phase of +3 d. Additional observations were obtained over the subsequent month in JHK_s with the MMT & Magellan Infrared Spectrograph (MMIRS; McLeod et al. 2012) on the Magellan Clay Telescope. To follow the light curve in the rest-frame optical to late times, we obtained a series of JH observations using DD time on the 8-m Very Large Telescope (Yepun) with the High-Acuity Wide-field K-band Imager (HAWK-I; Kissler-Patig et al. 2008). Finally, we used the FourStar Infrared Camera (Persson et al. 2008) on the Magellan Baade telescope to obtain late-time JHK_s observations of the host galaxy of PS1-10afx on 2011 September 18, 2011 September 21, and 2011 December 7, respectively.

The images were flat fielded, sky subtracted, and stacked using standard tasks in IRAF, including the `gemini` package for the NIRI data, except for the HAWK-I data, which were processed using the instrument pipeline. The images from each instrument were then calibrated using the same 2MASS stars in each field, except for the Y image, which was calibrated using archival NIRI zeropoints. The H and K_s host galaxy fluxes were then subtracted numerically from each datapoint in those filters. For the Y data point, we interpolated the host galaxy flux between the measured values in y_{P1} and J to subtract off the host galaxy contribution (only a small correction). We were able to perform image subtraction on most of the J images using the ISIS software package with the late-time FourStar image as a template, but the others had the host J flux subtracted numerically.

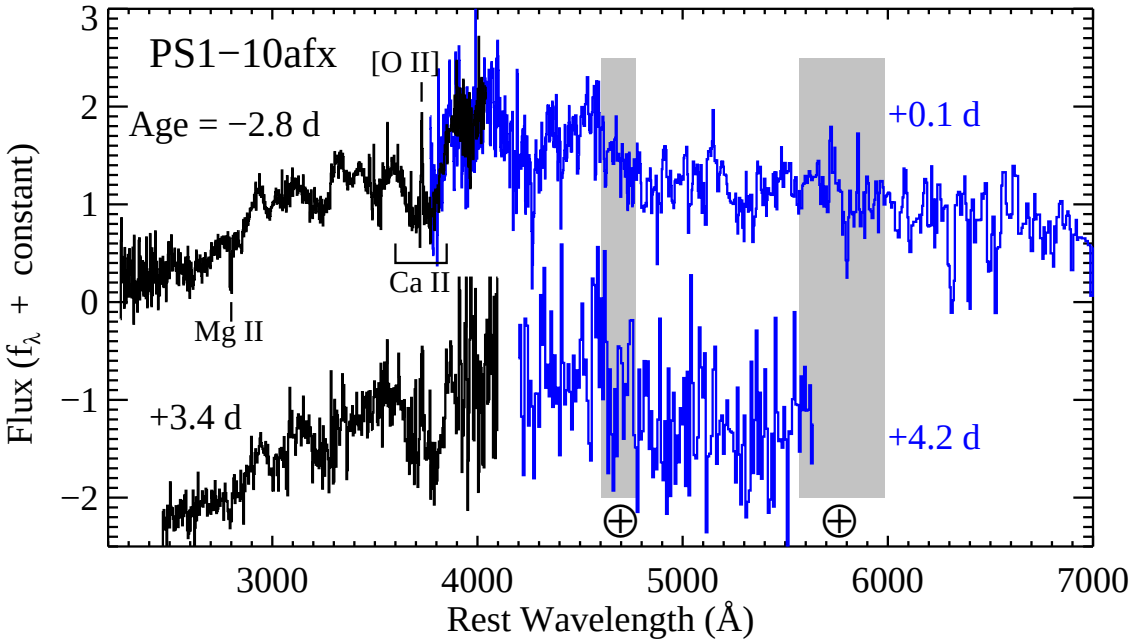

Figure 3. Optical (black) and NIR (blue) spectra of PS1-10afx. The spectra are labeled with their phase in rest-frame days. The O II λ3727 emission and Mg II λ2800 absorption from the host galaxy are labeled, as is the broad Ca II H+K P-Cygni feature from the SN itself. The zeropoint of the flux scale is appropriate for the day −2.8/+0.1 GMOS/FIRE spectra. The day +3.4/+4.2 GMOS/MMIRS spectra have been shifted down by 2.5 flux units. The gray bars labeled with a ⊕ symbol represent the regions of strong telluric absorption between Y/J and J/H.

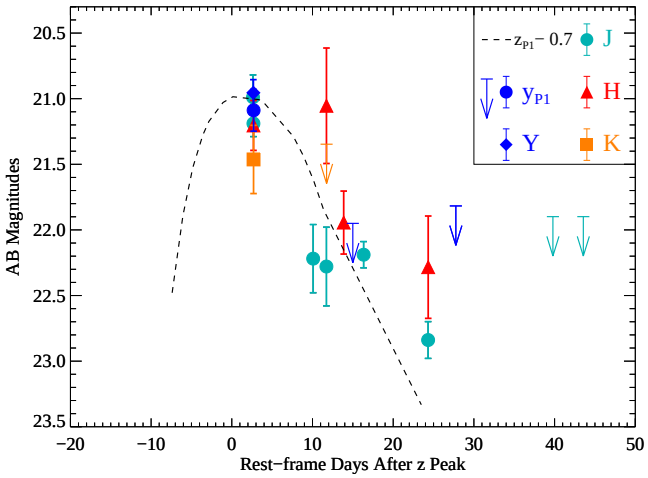

Figure 4. NIR photometry of PS1-10afx. The dashed line shows a polynomial fit to the well-sampled z_{P1} light curve to guide the eye, shifted by 0.7 mag to go through the J photometry near maximum light.

The final host-corrected photometry points are shown in Figure 4 and listed in Table 1, including the calibration uncertainty in the errors.

2.5. *NIR Spectroscopy*

We observed PS1-10afx with the Folded-port InfraRed Echellette (FIRE; Simcoe et al. 2008) spectrograph on the Magellan Baade telescope on 2010 September 18.17 (phase +0.1 d), using the high throughput, low-resolution prism mode to cover the range of 0.8−2.5 μm. The spectral resolution is a strongly decreasing function of wavelength, but is $R \approx 500$ in J. Six 150 s dithered exposures were obtained for a total of 900 s of on-source time. Despite the short exposure time, the continuum of PS1-10afx is well detected blueward of ∼1.6 μm. We reduced and combined the spectra using the FIREHOSE package, including a correction for telluric absorption obtained from observations of the A0V star HD 208368 using the algorithm of Vacca et al. (2003).

We obtained a MMIRS spectrum on 2010 September 28, using the zJ filter and J grism to cover the range 1.0−1.34 μm. A total of 90 minutes were spent on source in a series of dithered 300 s exposures. We used standard tasks in IRAF to combine and extract the spectra. The final NIR spectra are shown in Figure 3.

2.6. *Radio Observations*

Popular models for SLSNe do not predict detectable radio emission at high redshift, as discussed by Chomiuk et al. (2011). However, given its unusual properties, we observed PS1-10afx on 2010 September 12.2 (phase −2.4 d) with the Karl G. Jansky Very Large Array (Perley et al. 2011) as part of our NRAO Key Science Project "Exotic Explosions, Eruptions, and Disruptions: A New Transient Phase-Space," with 256 MHz of bandwidth centered at 4.96 GHz. The data were reduced with standard tasks in the Astronomical Image Processing System (AIPS; Greisen 2003), using J2212+0152 as the gain calibrator and 3C48 as the absolute flux density calibrator. These observations yielded a non-detection of 19±18 μJy.

3. HOST GALAXY OBSERVATIONS

We measure a host redshift of $z = 1.3883 \pm 0.0001$ from fits to the [O II] line in our highest S/N spectrum (phase −2.8 d). A double-Gaussian fit to the Mg II λ2800 doublet absorption in the same spectrum is blueshifted by 120±12 km s^{-1} relative to the [O II] rest frame.

Such an offset is typical of rest-frame UV selected star-forming galaxies at this redshift (Erb et al. 2012) and was also seen in observations of the SLSN PS1-11bam (Berger et al. 2012). This effect has been interpreted to be caused by absorption occurring in galactic-scale outflows driven by star formation. The rest-frame equivalent widths (W_r) of the two lines are $W_r(\lambda2796)$=1.8±0.2 Å and $W_r(\lambda2803)$=1.6±0.2 Å. These values are larger than for PS1-11bam (Berger et al. 2012), but slightly lower than the median of the intrinsic absorbers from gamma-ray burst (GRB) host galaxies (Fynbo et al. 2009). In addition, Mg I λ2852 absorption is present, but the UV spectral slope of PS1-10afx is so red that the S/N rapidly decreases to the blue, making it hard to confirm the presence of other expected strong interstellar absorption lines, such as Fe II λ2600.

We obtained photometry of the host galaxy of PS1-10afx in eight filters from g' to K_s (Table 2) to probe the host stellar population from the rest-frame NUV (∼2000 Å) to the NIR (∼0.9 μm). The host is well detected in our deep $i_{\rm P1}z_{\rm P1}y_{\rm P1}$ PS1 template images, which we supplemented with the observations from other facilities described above. Host photometry was performed with a consistent aperture of radius 1.7″ in all filters.

We fit a suite of single stellar population age models from Maraston (2005) to the data, assuming a red horizontal branch morphology, a Salpeter initial mass function, and a metallicity of $Z = 0.5\ Z_\odot$. The best-fit model is shown in Figure 5 and has an age of 10^8 yr and requires a small amount of internal extinction (A_V = 0.4 mag). The derived stellar mass is $\sim1.8 \times 10^{10}$ M$_\odot$. The g' magnitude of the host galaxy corresponds to a NUV continuum luminosity of 1.3×10^{29} erg s^{-1} (after correction for internal extinction), which implies a star formation rate (SFR) of ∼18 M$_\odot$ yr^{-1} using the calibration of Kennicutt (1998). We also estimate a consistent value of ∼13 M$_\odot$ yr^{-1} from the observed [O II] flux of $(4.7\pm0.5)\times10^{-17}$ erg cm^{-2} s^{-1} (Kennicutt 1998). These SFRs would be a factor of ∼2 lower without any correction for internal extinction.

The host is marginally resolved in our template images, with a full width at half-maximum (FWHM) of ∼1.″2, or 10 kpc at this redshift. Astrometric alignment of difference images taken near maximum light with the templates shows that PS1-10afx is aligned with the centroid of the host to within 0.″1 (0.8 kpc).

This galaxy is significantly more massive than the previous hosts of SLSNe. Neill et al. (2011) examined the host galaxies of a sample of luminous SNe and found them to have generally low stellar masses and high specific SFRs. In particular, all of the SLSNe-I in their sample had dwarf hosts, with a median stellar mass of $\sim2\times10^8$ M$_\odot$. By comparison, PS1-10afx has a significantly more massive host with a lower specific SFR ($\sim8\times10^{-10}$ yr^{-1}) than their sample (with a median of 3×10^{-9} yr^{-1}). Only the luminous host galaxy of the SLSN-II 2006gy exceeded our estimate for the stellar mass of the host of PS1-10afx. Objects discovered subsequently have continued this trend, having either dwarf host galaxies or no host at all detected to date despite deep observations (Quimby et al. 2011; Chomiuk et al. 2011; Leloudas et al. 2012; Chen et al. 2013; Lunnan et al. 2013).

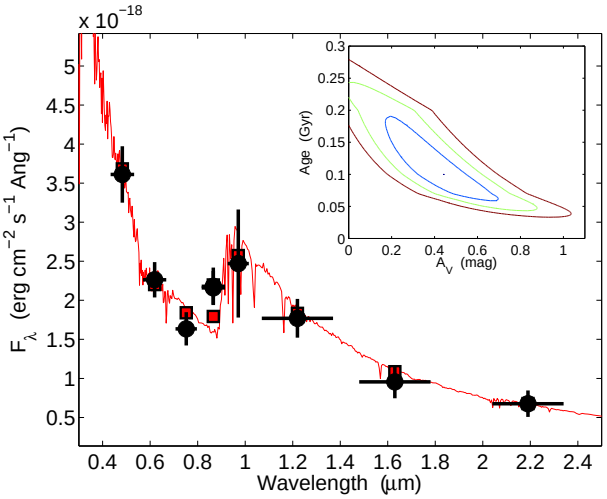

Figure 5. Host galaxy SED. The black data points represent the observed host galaxy photometry (Table 2), corrected for the derived $A_V = 0.4$ mag of internal reddening, and plotted versus observed wavelength. The filled red squares show the expected fluxes of the best-fit model (red line) in each of the observed bandpasses. The inset shows the 1, 2, and 3σ contours for the best fit in the host reddening-age plane.

While it has been argued that the association of SLSNe with dwarf galaxy hosts is driven by their low metallicity (e.g., Neill et al. 2011), the massive host of PS1-10afx appears to be inconsistent with a low metallicity. For example, the relationships of Mannucci et al. (2010) imply a super-solar metallicity of $12+\log({\rm O/H}) = 8.85$ for our derived stellar mass and SFR, although we caution that we cannot measure the metallicity directly with the available data. An additional point of contrast is provided by the sample of long-duration GRBs, whose occurrence is also widely believed to be associated with low-metallicity environments (e.g., Stanek et al. 2006). The host galaxy of PS1-10afx is brighter in K_s than any of the GRB host galaxies at similar redshifts in the optically-unbiased sample of Hjorth et al. (2012), although a few of the "dark" GRB hosts studied by Perley et al. (2013) are similarly luminous.

The absolute magnitudes of PS1-10afx's host prior to any internal extinction correction, $M_{2800\text{Å}} \approx -20.3$ mag and $M_B \approx -21.7$ mag, are ∼0.4 mag brighter than M^*, the characteristic magnitudes in Schechter (1976) function fits to the field galaxy luminosity functions at this redshift (Gabasch et al. 2004; Faber et al. 2007). The K_s magnitude of the host is also near the median of the distribution of field galaxies at this redshift weighted by star formation rate (Kajisawa et al. 2010). Combined, these points suggest that the environment of PS1-10afx is representative of typical star-forming galaxies at this redshift, while being distinct from the other hydrogen-poor SLSNe.

4. SPECTROSCOPIC COMPARISONS

Despite its extraordinary luminosity (see Section 5), PS1-10afx has spectra that more closely resemble those of a normal SN Ic than any known SLSN. We show our highest S/N spectrum (phase −2.8 d) in Figures 6 and 7 along with several comparisons drawn from the literature. Relatively few UV spectra of core-collapse SNe exist, but the available data allow us to sample a wide

Table 2
PS1-10afx Host Galaxy Photometry

Filter	Observed/Rest-frame Wavelength (Å)	Magnitude[a] (AB)	Error	Instrument
g'	4825/2020	24.01	0.10	LDSS3
r'	6170/2580	23.69	0.10	LDSS3
$i_{\rm P1}$	7520/3150	23.43	0.13	PS1
$z_{\rm P1}$	8660/3625	22.75	0.10	PS1
$y_{\rm P1}$	9620/4030	22.29	0.28	PS1
J	12500/5230	22.02	0.14	FourStar
H	16500/6910	21.93	0.22	FourStar
K_s	21490/9000	21.53	0.25	FourStar

[a] Corrected for Galactic extinction.

variety of phenomena. The most prominent feature in the PS1-10afx spectrum is a broad P-Cygni feature with an absorption minimum near 3730 Å, which we identify as the typical Ca II H&K absorption seen in most types of SNe, blueshifted by about 16,000 km s^{-1}. There are several other weaker features in the spectrum in the range 3000−3500 Å. The +3.4 d GMOS spectrum is noisier, but similar, with some evidence that the broad Ca II absorption minimum decreased in velocity, although the overlapping [O II] emission and strong night sky residuals make this uncertain.

These spectra are in strong contrast to the SN 2005ap-like class of SLSNe (Quimby et al. 2011). PS1-10ky is a high-redshift example of this class (Chomiuk et al. 2011) and it has a much bluer NUV continuum with no Ca II feature (Figure 6). A reasonable concern is that PS1-10afx only appears to have redder colors due to host-galaxy extinction. However, matching the UV spectral slope of PS1-10afx to PS1-10ky requires $E(B-V) \approx 1$ mag of extinction (gray line in Figure 6), assuming a Galactic reddening curve (Cardelli et al. 1989). This is unsatisfactory for two reasons. First, PS1-10afx is already more luminous in the NUV than the SN 2005ap-like objects (see below), so $A_u \approx 4.7$ mag would imply an upward correction of two orders of magnitude to an already extreme peak luminosity. Second, the strongest UV spectral features of the SN 2005ap-like objects are the trio of features blueward of 3000 Å first seen in SCP06F6 (Barbary et al. 2009), with the continuum redward of that being largely smooth except for O II features (Quimby et al. 2011). PS1-10afx has fundamentally different spectral features with no correspondence in the PS1-10ky spectrum, so the simplest explanation is that it has an intrinsically cooler photosphere.

The SN IIn 1998S is shown in Figure 6 as a well-studied example of a SN undergoing strong CSM interaction. SN 1998S at this phase showed no broad P-Cygni features in the UV, but had a blue continuum with narrow absorption lines from interstellar and circumstellar material (Fransson et al. 2005). The SLSNe 2006gy and 2006tf are higher-luminosity versions of SNe dominated by hydrogen-rich CSM interaction (Ofek et al. 2007; Smith et al. 2007, 2008, 2010). These objects have redder spectra than SN 1998S, but still exhibit Balmer lines and deep narrow absorptions that have no analog in the PS1-10afx spectrum. The SLSN 2008es had almost featureless blue spectra near maximum light (Miller et al. 2009; Gezari et al. 2009), but the plotted spectrum is from a later epoch when Balmer lines were beginning to develop strength in the rest-frame optical spectrum.

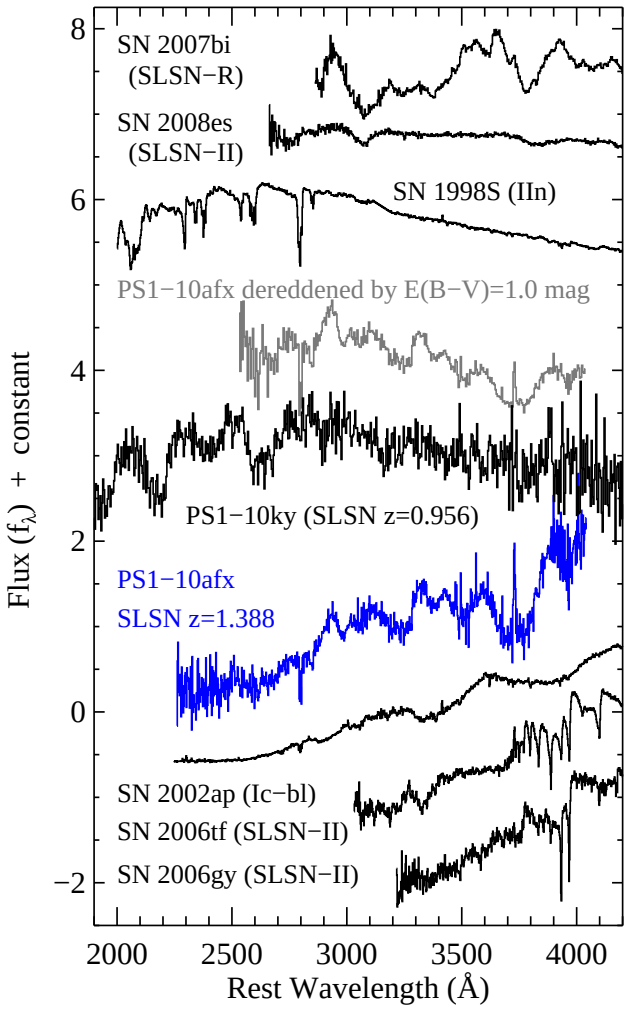

Figure 6. SLSNe and other NUV spectral comparisons for PS1-10afx (blue; −2.8 d). None of these objects is a good match to PS1-10afx. The spectrum in gray is the same one of PS1-10afx after correction for $E(B-V) = 1.0$ mag of reddening (see text for details). The other spectra and their phases relative to maximum light are: SN 2007bi (+54 d; Gal-Yam et al. 2009), SN 2008es (+21 d; Miller et al. 2009), SN 1998S (+14 d; Fransson et al. 2005), PS1-10ky (−2 d; Chomiuk et al. 2011), SN 2002ap (+4 d; data retrieved from the *Hubble Space Telescope* [*HST*] archive), SN 2006tf (+64 d; Smith et al. 2008), and SN 2006gy (+23 d; Smith et al. 2010). All literature data are corrected for Galactic and host reddening, if known.

The NUV spectrum of the broad-lined SN Ic 2002ap is included because the engine-driven SNe associated with GRBs have similar spectra, even if 2002ap itself was not unusually luminous (Mazzali et al. 2002). SN 2002ap has much broader and more blended features than PS1-10afx. Thus, none of these objects in Figure 6 resembles PS1-10afx. The SLSN 2007bi has been identified as a potential pair-instability SN (Gal-Yam et al. 2009; Young et al. 2010). It is more similar to PS1-10afx, with a definite Ca II feature, but is still significantly bluer and has several additional spectral features that do not match.

Instead, the set of spectra from normal SNe plotted

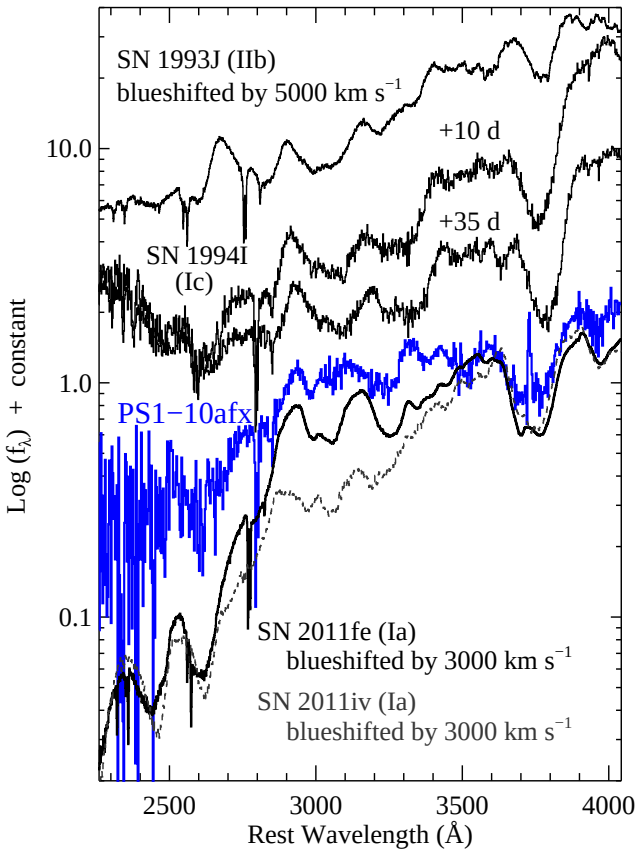

Figure 7. Normal SNe NUV spectral comparisons for PS1-10afx (blue; −2.8 d). These objects are much better matches than the ones shown in Figure 6. The other spectra and their phases relative to maximum light are: SN 1993J (−1 d; Jeffery et al. 1994), SN 1994I (+10 d and +35 d; data retrieved from the *HST* archive), and two SNe Ia, SN 2011fe (+0 d; Maguire et al. 2012; Foley 2013) and SN 2011iv (+0.6 d; Foley et al. 2012). The SNe Ia and SN 1993J spectra have been blueshifted to approximately match the absorption minima of the Ca II feature. All literature data are corrected for Galactic and host reddening, if known.

in Figure 7 provide a much better basis for comparison. The SNe Ia and SN 1993J (Type IIb) spectra have been blueshifted by the indicated amounts to approximately match the Ca II absorption minima to PS1-10afx. Over the range 2800−4000 Å, the spectra in Figure 7 are all very similar, with the dominant features being due to Ca II in all objects. A notch near 3950 Å is from Si II λ4130. An emission peak at 2900 Å also appears to be common to these objects, along with a bluer peak near 3150 Å. Shortward of ∼2800 Å, the SNe Ia diverge from the core-collapse objects. This dropoff in flux, along with a pair of deep absorption features near 2450 Å and 2600 Å, is caused by iron-group elements, primarily Co II (Kirshner et al. 1993; Sauer et al. 2008). The lack of these features in PS1-10afx is evidence that the abundance of newly-synthesized ^{56}Ni (which decays to ^{56}Co) near the photosphere is much lower than in a SN Ia.

One purpose of these comparisons is to demonstrate the apparent broad similarity of the NUV spectra of PS1-10afx to those of SNe coming from three very different progenitors: a bare core of a massive star (SN 1994I: Wheeler et al. 1994; Iwamoto et al. 1994), a partially-stripped massive star in a binary system that retained part of its hydrogen envelope (SN 1993J: Nomoto et al. 1993; Podsiadlowski et al. 1993; Woosley et al. 1994), and the thermonuclear explosions of white dwarfs (SNe 2011fe and 2011iv: Nugent et al. 2011; Foley et al. 2012). SNe 2011fe and 2011iv have some spectral differences from each other near 3000 Å, exhibiting the potential for spectroscopic variation in objects with similar progenitors. Other than the lack of cobalt near the photosphere, the remaining differences between PS1-10afx and these other objects are relatively minor.

In addition, the overall UV spectral slope of PS1-10afx is very similar to those of SNe 1993J and 1994I, after correction of both by $E(B-V) = 0.30$ mag of reddening (Richmond et al. 1994; Sauer et al. 2006). The fact that the only SNe in Figures 6 and 7 that have similar spectral features to PS1-10afx also have similar SED shapes provides further evidence that the extinction of PS1-10afx is not large. If the PS1-10afx spectra were corrected for a large amount of reddening, they would be bluer and we would expect different spectral features to be present at the higher implied temperatures.

We further explore the spectra using the SN spectrum synthesis code `SYN++` with `SYNAPPS` (Thomas et al. 2011) to fit the near-maximum-light GMOS/FIRE spectra. These codes are based on the same assumptions as the original `SYNOW` (e.g., Branch et al. 2002) treatment of resonant-scattering lines in the Sobolev approximation above a sharp photosphere that emits as a blackbody (BB). The atomic and ionic species are assumed to have levels populated in local thermodynamic equilibrium at some excitation temperature. `SYNOW` is a tool designed for line identifications and is not a full self-consistent spectral model.

Our best `SYNOW` model is shown in Figure 8 and contains seven ions. We assumed equal BB continuum and excitation temperatures of 10,200 K and a photospheric velocity of 11,000 km s^{-1}. The deep absorption trough near 3700 Å is dominated by Ca II H&K. Fe II and Ti II combine to produce several of the wiggles observed in the range 3000 − 3500 Å. Mg II naturally explains the observed absorption near 4250 Å, while also producing absorption shortward of ∼2700 Å. Si II contributes to both the blue wing of the deep Ca II feature and the notch near 3950 Å. The feature near 3950 Å is present in the overlap between the GMOS and FIRE data and has a consistent strength that is significantly larger than in the synthetic spectrum. With `SYNOW`, we have to be careful not to overproduce absorption by the Si II λ6355 doublet because no strong feature is seen in the data, although the S/N and the spectral resolution become very poor in the observed-frame H. We introduce Fe III to help reproduce the wiggle near 5000 Å, but the identification is not unique and its presence is not required. In addition, we include Cr II to help suppress the UV flux. That ion does not contribute sufficiently strongly to any specific feature for us to make a positive identification, but it has been included in previous `SYNOW` models of SNe Ic (Millard et al. 1999) because of its expected strength in either helium or carbon/oxygen-rich SN ejecta at these temperatures (Hatano et al. 1999).

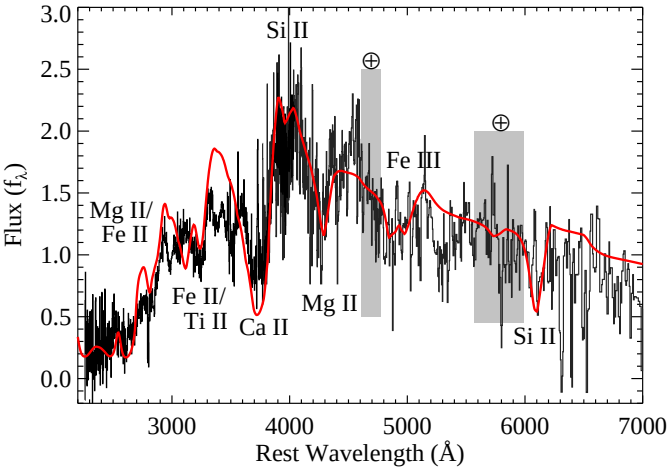

Figure 8. SYNOW fit for PS1-10afx (red) compared to the −2.8/+0.1 d GMOS/FIRE combined spectrum. Ions dominating major spectral features in the SYNOW model are indicated. The gray bars labeled with a ⊕ symbol represent the regions of strong telluric absorption.

We also consider several other species that were not included in the final fit. As discussed above, Co II produces strong NUV absorptions in SNe Ia that are not present in PS1-10afx. Na I D is commonly seen in all types of SNe, but at this redshift it would fall in the strong telluric absorption between J and H, so we have no constraint on its presence from the observations. We also tested Sc II because of its use in prior SYNOW analyses of SNe Ib (Branch et al. 2002). Scandium results in an additional absorption minimum near ∼3500 Å similar to one seen in our data, but does not produce a sufficiently strong improvement in the model to justify its inclusion, particularly given the expectation that it should only become important at lower ejecta temperatures (Hatano et al. 1999). Lines of hydrogen or helium would be very important if present, but there is no evidence for either, although the low S/N of our NIR data precludes strong statements about helium. The SN 2005ap-like SLSNe have lines of singly-ionized carbon and oxygen in their spectra at early times (e.g., Quimby et al. 2011), with possible contributions from doubly-ionized CNO elements (Pastorello et al. 2010), but those lines do not appear to be present in our PS1-10afx spectra.

Overall, we can reproduce the shape of the spectrum in the rest-frame optical reasonably well, but the NUV is more problematic. Our synthetic spectrum has features at many of the same wavelengths as the real data, but the overall shape in the NUV is less well fit. Adding additional ions to the fit might potentially help the UV shape of the synthetic spectrum, but would not be well motivated or add any additional insight. Alternatively, the radiative transfer in the UV is known to be complex and we could be encountering the limitations of SYNOW. There is also an apparent absorption feature near 5300 Å that is not fit by the model. The most important point is that the ions we have used are typical for generic fits to SNe Ia and Ic spectra (e.g., Branch et al. 2002), but differ from those identified in most SLSNe-I spectra near maximum light (Quimby et al. 2011; Chomiuk et al. 2011; Leloudas et al. 2012; Lunnan et al. 2013).

5. LIGHT CURVE AND ENERGETICS

Existing light curves of SLSNe are heterogeneous, and the objects have been found at a wide range of redshifts, making direct comparisons difficult. Following previous work (Quimby et al. 2011; Chomiuk et al. 2011; Lunnan et al. 2013), in Figure 9 we compare the rest-frame u light curve of PS1-10afx (corresponding to observed-frame $z_{\rm P1}$) to several of the most luminous SN 2005ap-like SNe in the literature. In addition, we include the hydrogen-rich SN 2008es because its light curve is similar to the others and it did not develop strong Balmer lines until well after maximum light (Miller et al. 2009; Gezari et al. 2009). For comparison, we also plot the U light curves of the broad-lined SNe Ic 1998bw and 2002ap, two objects of normal luminosities (Galama et al. 1998; Foley et al. 2003). Given the uncertain SEDs of many of these objects, we do not perform a full k-correction, but instead correct the observed AB magnitudes in filters whose effective wavelengths are close to u in the observed frame by $m - M = 5\log(\mathrm{d}_L(z)/10\ \mathrm{pc}) - 2.5\log(1+z)$, where d_L is the luminosity distance. To be conservative, we assume that PS1-10afx is unaffected by reddening here and in all following discussion, despite the strong Mg II absorption along the line of sight and the inference that the host galaxy SED requires some degree of internal extinction. We presented some evidence above that the reddening to the SN is not large, but it is possible that we have underestimated the peak luminosity of this object.

It is apparent from Figure 9 that at peak PS1-10afx was slightly more luminous in u ($M_u \approx -22.3$ mag) than any previous SLSNe. However, by ∼10 d on either side of maximum light, PS1-10afx falls below all the others. This emphasizes the high peak luminosity and fast evolution of the light curve. These objects have rather different SEDs, so comparisons of the energetics require constructing a bolometric light curve.

To proceed further, we first construct SEDs at three epochs near the times of our NIR observations, at phases of +3, +12, and +24 d. We fit third-order polynomials to the observed photometry in each $r_{\rm P1}i_{\rm P1}z_{\rm P1}$ filter around each SED epoch to estimate the flux. We then estimate the error bars on these fitted fluxes by generating Monte Carlo realizations of the data where we repeatedly randomly adjust the observed fluxes by drawing from a normal distribution having a width of the measured errors, refitting, and determining the variance of the interpolated flux at the desired epoch. We perform a similar procedure whenever we need to interpolate fluxes to a common epoch. For the SEDs at phases of +3 and +24 d, we use the actual measured $y_{\rm P1}$ and NIR fluxes. For the +12 d SED, the observed NIR fluxes were quite noisy, so we again interpolate the fluxes in J and H by fitting second-order polynomials to the observed light curves to generate the points on the SED. The resulting SED evolution is shown in Figure 10.

We then fit BB spectra to the SEDs at each epoch. Our +3 d SED has the most complete information. The dashed line in Figure 10 shows the result of a BB fit to the full SED. The derived BB temperature is $T_{\rm BB} \approx 6800$ K, but clearly the curve is a poor fit to the data at rest wavelengths longward of ∼5000 Å. If instead we restrict the fit to $y_{\rm P1}$ and the NIR bands, the BB temperature is

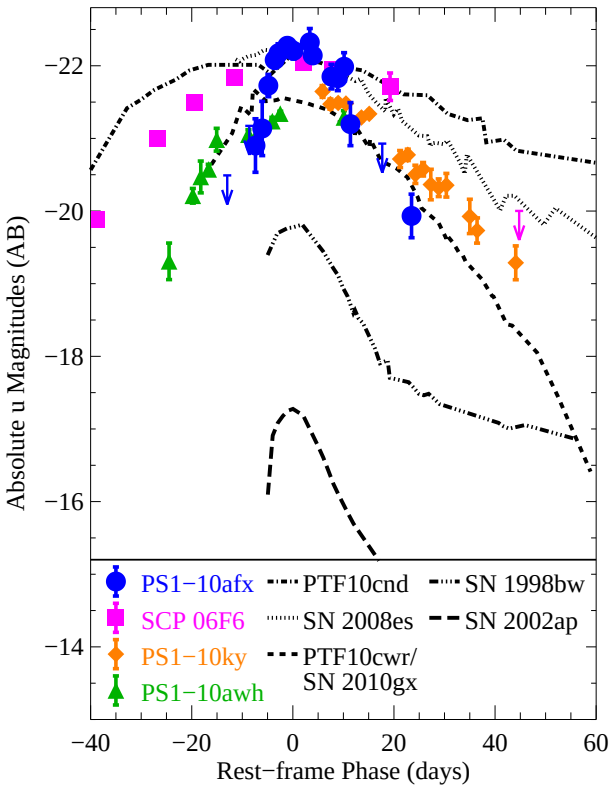

Figure 9. Absolute u light curves of PS1-10afx and other SNe. The observed bands and wavelengths in the rest frame are: PS1-10afx (z_{P1}, 3525 Å), SCP 06F6 (F850LP, 3883 Å; Barbary et al. 2009), PS1-10ky (i_{P1}, 3848 Å; Chomiuk et al. 2011), PS1-10awh (i_{P1}, 3944 Å; Chomiuk et al. 2011), PTF 09cnd (rest-frame u from Quimby et al. 2011), SN 2008es (B/g, 3604 Å; Miller et al. 2009; Gezari et al. 2009), SN 2010gx/PTF 10cwr (g, 3770 Å; Pastorello et al. 2010; Quimby et al. 2011), SN 1998bw (U, 3663 Å; Galama et al. 1998), and SN 2002ap (U, 3663 Å; Foley et al. 2003).

not well constrained ($T_{BB} = 12,000 \pm 2,000$ K) due to a lack of points blueward of the peak. The formal best fit is plotted as the solid blue line in Figure 10 and provides a much better fit to the NIR data points (by construction), but significantly overestimates the rest-frame UV flux. This is to be expected if line blanketing in the NUV provided by iron-peak elements supresses the UV flux, as is typical for SNe Ic. For example, the shape of the SED of the normal SN Ic 1994I near maximum light (Figure 10) is similar to that of PS1-10afx, but the detailed model fits by Sauer et al. (2006) find an underlying BB temperature of 9230 K at the same epoch.

The data at phases +12 and +24 d are less complete, so we fit a simple BB to all of the points on the SED and do not correct for line blanketing, which would only be expected to increase as the ejecta cool. The derived BBs show the ejecta clearly cooling from $\sim 12,000$ K at a phase of +3 d to ~ 5500 K at +24 d, although T_{BB} should only be regarded as lower limits to the effective temperature (T_{eff}) on the later two dates. Independent of the details of line blanketing, we can directly see the SED becoming redder, and hence implying cooler temperatures, by looking at the color evolution. In Figure 11, we construct $i_{P1}-z_{P1}$ and $z_{P1}-J$ color curves.

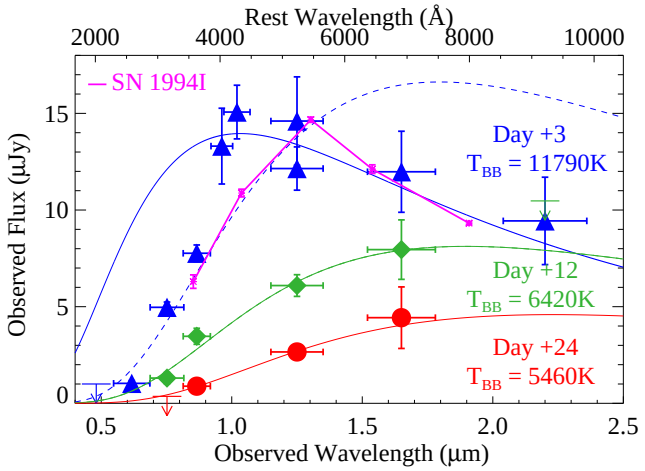

Figure 10. SED of PS1-10afx at three epochs, phases of +3 (blue triangles), +12 (green diamonds), and +24 d (red circles). The solid lines are BB fits to the SED at each epoch. At a phase of +3 d, the blue dashed line is a fit to all data points, while the solid line excludes $g_{P1}r_{P1}i_{P1}z_{P1}$ from the fit. Reported BB temperatures are in the rest frame. The magenta line shows the SED of SN 1994I near maximum light shifted to the redshift of PS1-10afx and arbitrarily scaled to match the flux level. The 1994I data points are the $UBVRI$ photometry on 1994 April 5.39 from Richmond et al. (1996) corrected for $E(B-V) = 0.3$ mag (Sauer et al. 2006) of reddening.

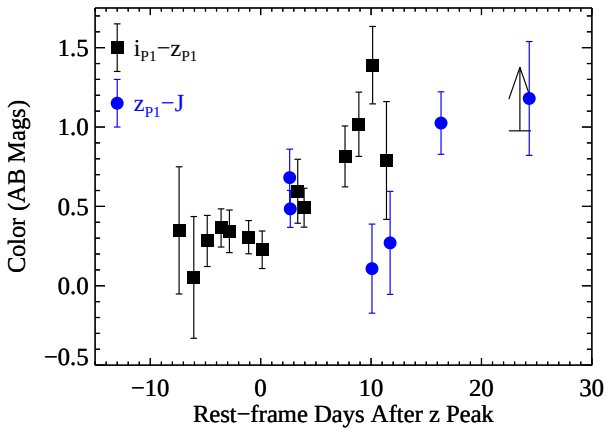

Figure 11. Observed color evolution of PS1-10afx. At this redshift, z_{P1} is near rest-frame u band and J is near V, while i_{P1} is in the NUV. Note the flat $i_{P1}-z_{P1}$ color prior to maximum light.

In each case, we interpolate the light curve in the bluer band to the epochs of observation for the noisier redder band. The $i_{P1}-z_{P1}$ color is consistent with a constant (0.30±0.05 mag) before maximum light, but both colors became redder with time after maximum.

We use the BB fits to construct a bolometric light curve, starting with the near-maximum-light SED (phase +3 d) shown in Figure 10. A trapezoidal integration of the observed fluxes from r_{P1} to K gives a minimum bolometric luminosity (L_{bol}) near peak of $(3.6\pm0.2)\times10^{44}$ erg s^{-1}. To account for flux emitted redward of our observations, we add the tail of the BB and extend the trapezoidal integration to long wavelengths, which provides only a 14% upward correction to the total flux. We repeat the process for the other

two SED epochs. After including the BB tails, the derived bolometric luminosities are (4.1±0.2), (2.2±0.2), and (1.1±0.3)×10^{44} erg s^{-1} at phases of +3, +12, and +24 d, respectively.

Although we lack NIR data at other epochs, we can use these fits to estimate the bolometric light curve in combination with the well-sampled PS1 light curves. For each of our three SED epochs, we define a multiplicative bolometric correction factor to obtain $L_{\rm bol}$ from νL_ν in the $z_{\rm P1}$ band. Motivated by the lack of strong color evolution before maximum light, we apply the bolometric correction factor from +3 d to all pre-maximum $z_{\rm P1}$ data points. For the post-maximum data, we use a smoothly varying time-dependent correction factor to evolve from the +3 d value to the +24 d value. We repeat the process for the $i_{\rm P1}$ band, except that we use a smaller (but constant) bolometric correction factor before maximum light than the derived +3 d value to better match the $z_{\rm P1}$ results and account for the small amount of $i_{\rm P1}-z_{\rm P1}$ color evolution between +3 d and the pre-maximum data. The combined bolometric light curve is plotted in Figure 12. A third-order polynomial fit to the peak of the bolometric luminosity curve gives a maximum value of (4.1±0.1)×10^{44} erg s^{-1}, equivalent to 1.1×10^{11} L$_\odot$, not including the uncertainty in the bolometric correction factors (or potential extinction).

To check that our derived maximum bolometric luminosity of PS1-10afx is realistic and that our procedure for extrapolating the SED to the NIR has not introduced any significant error, we can take advantage of the fact that the shapes of the spectra we have of PS1-10afx and the derived SEDs are very similar to those of a SN Ia near maximum light (cf. Figure 7). One of the most distant spectroscopically confirmed SNe Ia known, HST04Sas, is at $z = 1.39$ (Riess et al. 2007), consistent with the redshift of PS1-10afx. Interpolating the F850LP ($\sim z$ band) light curve of HST04Sas to a phase of zero days produces an estimate of the observed magnitude of $m_{F850LP}(t = 0) = 25.5$ mag (AB), while fits to PS1-10afx show that $z_{\rm P1}(t = 0) = 21.7$ mag. Assuming that the similarity of the SEDs requires no further correction factors and a typical SN Ia peak bolometric luminosity of ∼1.2×10^{43} erg s^{-1} (e.g., Stritzinger et al. 2006), the 3.8 mag difference between the objects corresponds to a peak bolometric luminosity for PS1-10afx of $L_{\rm bol} \approx 4\times10^{44}$ erg s^{-1}, in excellent agreement with our value derived above.

In fact, the peak of $M_{\rm bol} = -22.8$ mag is more luminous than any of the hydrogen-poor objects collected by Gal-Yam (2012)[15]. This statement is somewhat uncertain due to the heterogeneous and fragmentary nature of the available data for SEDs and bolometric correction factors for the objects in the literature. SNe 2008es (Miller et al. 2009; Gezari et al. 2009), 2005ap (Quimby et al. 2007), and SCP06F6 (Barbary et al. 2009; Quimby et al. 2011) all have similar peak bolometric luminosities to PS1-10afx, but the exact comparison depends on the treatment of the bolometric correction for these UV-luminous sources. The only SLSN of any type with a clearly higher peak luminosity is the peculiar hydrogen-rich transient CSS100217 (Drake et al. 2011).

[15] For consistency, we note that using the same cosmology as Gal-Yam would result in $M_{\rm bol} = -22.9$ mag.

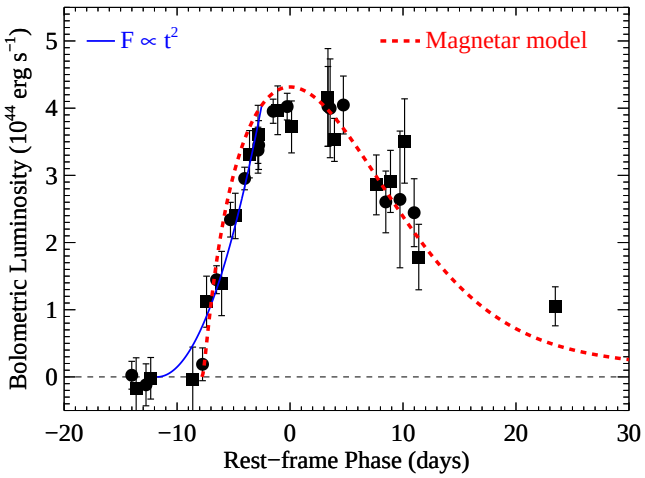

Figure 12. Bolometric light curve of PS1-10afx. The observed $i_{\rm P1}$ (circles) and $z_{\rm P1}$ (squares) light curve points were multiplied by a time-dependent bolometric correction factor (see text for details). The plotted error bars only represent the nominal photometric errors and do not include any contribution from the systematics of converting to bolometric luminosities. The solid blue line shows a fit to the early-time flux that rises as t^2. The red dashed line shows a model for a SN powered by the dipole spindown energy from a magnetar, following Kasen & Bildsten (2010). We assume an opacity of 0.2 cm^2 g^{-1}, 1 M$_\odot$ of ejecta, 10^{51} erg of kinetic energy in the initial SN, an initial magnetic field strength of 6×10^{14} G, and an initial magnetar spin period of 2 ms. This model predicts high temperatures and velocities that are in contradiction of the data despite the apparent good fit. See Section 6.2 for further discussion.

However, the SN nature of that object is still questionable due to possible confusion with the active galactic nucleus of its host galaxy.

We pause to consider whether gravitational lensing could result in an object with the spectrum and light curve shape of a normal SN Ic, but artificially boosted in luminosity. However, the peak luminosity of PS1-10afx is a factor of $\gtrsim$50 higher than normal SNe Ic, requiring an extremely high magnification factor despite the lack of an obvious lens. There is no foreground galaxy cluster visible in the PS1 images, and the source present along the line of sight to PS1-10afx exhibits [O II] emission and the SED of a galaxy at the same redshift as the SN, consistent with just being the host. Therefore, we do not consider this hypothesis further.

In addition to the high peak luminosity of PS1-10afx, another striking fact about the light curve is the rapid time evolution. Despite the rolling survey nature of PS1, our first detection is at a phase of only −7.4 d, with non-detections prior to that (Figure 12). It is traditional in SN studies to find the rise time by fitting a fireball model of the form $L_{\rm bol} \propto t^2$ for $t > t_0$ at early times, where t_0 is the explosion time. For PS1-10afx, this gives a $t_0 = -11.8 \pm 0.7$ d (Figure 12). Allowing the power-law index to vary gives a best fit with $L_{\rm bol} \propto t^{0.9\pm0.5}$ and $t_0 = -8.7 \pm 1.9$ d. Regardless of the exact parameterization, the rise in $z_{\rm P1}$ is a factor of 3.5 in flux in the 7.4 d before peak. This apparent rise time is much faster than the fastest known SLSNe (Figure 9; Quimby et al. 2011; Pastorello et al. 2010; Leloudas et al. 2012; Lunnan et al. 2013).

The decay timescale is also unusually fast. The FWHM of the bolometric light curve is only 18 d. The usual

parameterization of SN light curve shapes, Δm_{15}, is the decline in magnitudes in 15 d after maximum light. The bolometric light curve of PS1-10afx has Δm_{15}=0.95 mag. By comparison, only SN 1994I has a faster $\Delta m_{15}(R)$ in the collection of SNe Ib/c light curves of Drout et al. (2011), although several additional objects had $\Delta m_{15}(V)$ that are comparable. Figure 9 demonstrates that in u, PS1-10afx also has a faster light curve decay than SLSNe of similar peak luminosity.

Integrating the observed bolometric light curve from the first detection at a phase of −7.4 d to the last detection at +24 d provides a lower limit on the emitted energy of $\sim 7\times10^{50}$ erg (over only 31 d). Reasonable extrapolations of the light curve to later times will increase the total to $\sim 10^{51}$ erg, comparable to most other hydrogen-deficient SLSNe, but not notably high (e.g., Quimby et al. 2011; Chomiuk et al. 2011). The fast timescale of PS1-10afx compensates for its high peak luminosity.

6. COMPARISON TO MODELS

The difficult constraints placed by the rise time on any model can be seen from the inferred emitting radius. Assuming $T_{\rm eff} \approx 11,790$ K as derived above, the BB radius ($R_{\rm BB}$) of the photosphere at maximum light is 5.5×10^{15} cm. This is larger than for other hydrogen-poor SLSNe, which typically have inferred radii of $\sim 10^{15}$ cm (Quimby et al. 2011; Chomiuk et al. 2011), as expected from the higher luminosity and lower $T_{\rm BB}$ of PS1-10afx. If $T_{\rm eff}$ is actually as low as the color temperature of ∼6800 K, then the inferred radius at maximum light increases to 1.6×10^{16} cm.

The most conservative set of numbers at maximum light ($R_{\rm BB}$=5.5×10^{15} cm, t_0=−11.8 d) requires an expansion velocity of ∼50,000 km s^{-1} if t_0 is the true explosion time, in obvious conflict with the observed photospheric velocities seen in the spectrum. Material moving at the SYNOW-derived velocity of 11,000 km s^{-1} will take 58 d to reach that radius, implying an explosion ∼50 d before our first detection. There is an observed example of such an effect with the SLSN 2006oz. It exhibited a precursor plateau with a luminosity of $\sim 2\times10^{43}$ erg s^{-1} prior to rising to the main peak of the light curve, which Leloudas et al. (2012) interpreted as being due to a recombination wave in an oxygen-rich CSM. A weighted average of the PS1-10afx non-detections between phases −15 and −8 d produces a mean luminosity of $(0.2\pm1.2)\times10^{43}$ erg s^{-1}. At the 2σ level, this non-detection is consistent with a hypothetical plateau being present at the level seen in SN 2006oz, but unobserved due to the limiting magnitudes of our survey.

At phases +12 and +24 d, the $L_{\rm bol}$ quoted above and $T_{\rm BB}$ shown in Figure 10 combine to produce BB radii of 1.4 and 1.3×10^{16} cm, respectively, although these are likely overestimated due to the underestimate of $T_{\rm eff}$ caused by line blanketing. Notably, these values are consistent with the photosphere begining to recede through the ejecta (in both the physical and comoving senses) as they become optically thin. By contrast, the BB radii inferred for the interacting SLSNe 2006tf and 2006gy increased linearly with time at the same rate as the velocities measured from the spectra, consistent with an expanding optically-thick shell (Smith et al. 2008, 2010). Although the measurement errors make it less certain, this also appears to be true for at least some SN 2005ap-like SNe (e.g., Chomiuk et al. 2011; Lunnan et al. 2013).

6.1. *Models Powered by Interaction*

The kinetic energy of a powerful SN explosion provides an attractive reservoir of energy to power SLSN light curves, but only if that energy can be efficiently converted to radiation. For PS1-10afx, this already requires an initial SN energy of at least a $few\times10^{51}$ erg in order for the object to radiate 10^{51} erg and still have ejecta velocities as high as those observed. This generally requires a CSM with a mass comparable to that of the ejecta and a radius comparable to the photospheric radius at maximum light in order to maximize efficiency and not lose energy to adiabatic expansion (e.g., Ginzburg & Balberg 2012). Another attraction of interaction models is that the SN can explode well before the start of the optical rise of the SN if the CSM is sufficiently dense to trap radiation from the shock (Chevalier & Irwin 2011). This could greatly alleviate the conflict described above between the rise time, ejecta velocity, and photospheric radius.

The required CSM densities in these models are much larger than for well-studied examples at lower luminosity. Chevalier & Irwin (2011) have identified two regimes of interest when the CSM is this dense. If the radiation from the shock can escape while the shock is still interacting with the CSM, then the light curve will be broad and exhibit a slow decay after maximum light. Their model works well for the light curves of SLSNe like 2006gy. An additional consequence of this model is that there should be spectral signatures of the ongoing CSM interaction, such as emission lines from the unshocked CSM (e.g., Chugai 2001). Other luminous SNe IIn in the literature, such as SNe 2008fz (Drake et al. 2010) and 2008am (Chatzopoulos et al. 2011), with their blue continua and strong Balmer emission lines, can also be fit by similar models.

The much faster light curve of PS1-10afx and lack of strong emission lines imply a different regime, one where the outer radius of the CSM is comparable to or smaller than the diffusion length of photons from the shock. In this framework, the optical light we detect is then associated with the breakout of the shock from the outer radius of the CSM. In the context of a dense wind with a density profile that scales with radius as $\rho = Dr^{-2}$ out to a maximum radius of R_w, where D is a density normalization parameter, the total mass of the wind is $M = 4\pi R_w D$. In the models of Chevalier & Irwin (2011), D can be estimated from the diffusion timescale as $D = 1.28\times10^{16}$ $(t_d/{\rm days})$ g cm^{-1}, if we assume an ionized He-rich composition. We can approximate the diffusion timescale t_d by the rise time and set R_w to the BB radius at maximum light to produce an estimate of the wind mass of $5-10$ M$_\odot$. These values are only approximate, as Ginzburg & Balberg (2012) have shown that in the regime of interest, the analytic approximations are outside the range of validity and require true hydrodynamic calculations.

Models with shock breakout occurring in a dense, truncated wind can produce bolometric light curves with the desired peak luminosities and time scales, but it is unclear if this can be done consistently with the other information about the object. Ginzburg & Balberg (2012)

were able to approximately match the light curve shapes of the SLSNe 2010gx and 2005ap, but the derived $T_{\rm BB}$ were hard to match to the observations. A theoretical caveat is that the observed color temperature could deviate from $T_{\rm eff}$ if the shock is not in equilibrium when it breaks out (Nakar & Sari 2010). This deviation is caused by the nature of the opacity, and usually implies that the color temperature is hotter than the true $T_{\rm eff}$ (e.g., see Moriya et al. 2013 for models of 2006gy), which would in turn require that the photosphere be at even larger radii than we have found. This effect might then conflict with the fast timescale of the light curve, which otherwise is indicative of a more compact CSM (Chevalier & Irwin 2011; Ginzburg & Balberg 2012), but detailed modeling with radiative transfer is needed to correctly evaluate these concerns.

Further, a key component of the rising SN luminosity in the shock breakout models of both Chevalier & Irwin (2011) and Ginzburg & Balberg (2012) is that the temperature rises to a maximum near the peak of the light curve and declines thereafter. Although we lack full SED information on the rise of the light curve for PS1-10afx, the observed $i_{\rm P1} - z_{\rm P1}$ color shows no evolution prior to the peak of the light curve (Figure 11). Despite the interpretation uncertainties introduced by the possibilities of line blanketing or deviations from equilibrium, the evolution of $T_{\rm BB}$ after maximum light results in a noticeable reddening of the $i_{\rm P1} - z_{\rm P1}$ color. If $T_{\rm BB}$ were rising by a similar amount while the light curve rose to its peak, we would have been able to detect it.

A separate uncertainty is the origin of this CSM, which could not be produced by steady stellar winds due to the high required mass-loss rates and the unexplained truncation at R_w. Most theoretical work has focused on winds, but the material could also be in a shell (Smith & McCray 2007; Moriya & Tominaga 2012). Woosley et al. (2007) invoked a pulsational pair instability to produce shells of matter at the appropriate distances, but these require very massive stars. Other possibilities include common envelope ejection (Chevalier 2012) and instabilities in the late stages of stellar evolution (Quataert & Shiode 2012).

Another challenge for CSM interaction being the dominant contributor to the luminosity of PS1-10afx is the appearance of the spectra. Interaction-powered SNe convert the kinetic energy of the explosion into UV/optical continuum radiation, frequently reprocessing some of the continuum into strong emission lines from the dominant constituents of the CSM external to the expanding shock. The spectral comparisons in Figure 6 show several examples of objects consistent with this picture. However, PS1-10afx is even more luminous than those objects and yet shows P-Cygni features originating in the SN ejecta, including a deep Ca II absorption comparable to that seen in SN 1994I. The lack of strong emission lines from the CSM can be explained if the material has a sharp outer radius, but interaction sufficiently luminous to dominate the light curve should dilute and weaken spectral features from the ejecta due to the "top-lighting" effect (Branch et al. 2000), if not completely hide emission from the unshocked ejecta. For example, PTF 09uj is a candidate for being a lower-luminosity version of a shock breakout through a dense (hydrogen-rich) wind and, as expected, its spectra are very blue and lack strong P-Cygni features (Ofek et al. 2010). It is not clear how strong CSM interaction could dominate the luminosity of PS1-10afx without leaving spectral signatures.

In summary, existing CSM interaction models can match the gross photometric properties of PS1-10afx (peak luminosity, timescales), but only if the models have the freedom to assume the necessary CSM structure. The origin of such unusual CSM is not explained *a priori* in these models. In addition, the details of the SED, color evolution, and emitted spectra appear to be in conflict with the observations, although more detailed radiative transfer calculations are necessary to be confident in the model predictions, which are largely based on BB assumptions.

6.2. *Internal Energy Sources*

Normal hydrogen-deficient SNe have light curves powered by the diffusion of energy deposited by the radioactive decay of ^{56}Ni and ^{56}Co. The light curves of most SLSNe-I appear to fade too rapidly relative to their peak luminosities to have radioactively-powered ejecta (Quimby et al. 2011; Pastorello et al. 2010; Chomiuk et al. 2011), and PS1-10afx is no exception. With a rise time of 12 d, the peak bolometric luminosity requires a nickel mass of $\sim$14 $M_\odot$. However, making standard assumptions about the structure of the ejecta (Arnett 1982; Valenti et al. 2008; Drout et al. 2011) allows us to use the photospheric velocity of 11,000 km s^{-1} and light curve timescale of 12 d (assuming that the diffusion timescale is comparable to the rise time) to estimate the ejecta mass as $\sim$2 $M_\odot$, clearly in contradiction of the high nickel mass.

Another potential power source suggested for SLSNe is the spindown energy from a newly-born magnetar (Maeda et al. 2007; Woosley 2010; Kasen & Bildsten 2010; Dessart et al. 2012a). The high luminosity and fast rise of PS1-10afx stretch the existing models to the bounds of plausibility. Inspection of Figures 4 and 5 of Kasen & Bildsten (2010) shows that the light curve of PS1-10afx requires a magnetar solution to have a very fast initial spin period ($p \approx 1 - 2$ ms, near the breakup speed of a neutron star), a low ejecta mass ($\sim$1 $M_\odot$), and a high magnetic field ($\gtrsim few \times 10^{14}$ G). This is because the high luminosity requires a high spindown power, while the fast light curve requires both fast spindown times and short diffusion timescales. We examined magnetar-powered light curves using the formalism of Kasen & Bildsten (2010) and found parameters that produced light curves that approximately matched the shape of the bolometric light curve of PS1-10afx. One such model is plotted in Figure 12.

However, it is not clear whether this fit should be regarded as more than a numerical curiosity because the physical assumptions underlying the model break down. In the parameter range appropriate for PS1-10afx, the magnetar dipole spindown energy (5×10^{51} $(p/2$ ms$)^{-2}$ erg) dominates over the initial SN kinetic energy (assumed to be 10^{51} erg). The Kasen & Bildsten (2010) models make an ansatz that the entire spindown energy of the magnetar is simply thermalized spherically at the base of the SN ejecta and deposited into the internal energy. Because this process accelerates and heats the ejecta, the final kinetic energy, the peak luminosity, and

the temperature are coupled. The model plotted in Figure 12 predicts expansion velocities of $\gtrsim$25,000 km s^{-1}, in contradiction of the observed spectrum. In addition, the model predicts a radius at maximum light (from the ejecta velocity and rise time) that when combined with the luminosity implies a BB temperature in excess of 20,000 K (with strong evolution at other times). This contradicts the observed $T_{\rm BB}$ near maximum light and the constant red $i_{\rm P1}-z_{\rm P1}$ color during the rise of the light curve. We find that increasing the assumed SN kinetic energy relative to the spindown energy does not alleviate these issues because of the difficulty in simultaneously satisfying the constraints from the expansion velocity seen at maximum light (which implies a normal energy-to-mass ratio, and hence high mass if the initial SN energy is high) with the fast diffusion timescale (which requires a low mass).

The models of Woosley (2010) start from massive star progenitors and proceed through the explosions, but they only probe slower rotating, and hence less energetic, magnetars than those required for PS1-10afx. Dessart et al. (2012a) also examined explosion models for Type Ib/c SNe with the addition of a central energy source that mimicked the effect of a magnetar. They followed the effects of a central energy source on the ejecta produced by the explosion models and generated light curves and spectra. If the central energy source deposited $\sim10^{51}$ erg of energy, the resulting SNe had high velocities and were blue at maximum light, which appears promising for explaining the SN 2005ap-like class of SLSNe, but is very different from PS1-10afx. As noted above, the light curve of PS1-10afx requires even more energy input from the magnetar. Therefore, we disfavor magnetar models at this time.

Dexter & Kasen (2012) have proposed a scenario that shares some similarities with the magnetar model in that their model has a post-explosion internal energy source, in this case provided by fallback accretion onto a newly formed compact remnant, likely a black hole. Their suite of models can only match the fast timescale and high peak luminosity of PS1-10afx if the progenitor is a blue supergiant and the initial SN explosion energy is extremely low with an ejecta mass of $\sim$1 M$_\odot$. Their hydrogen-poor models do not reach the same peak luminosities, which is a problem for PS1-10afx. In addition, these models have the same problem as the magnetar ones in simultaneously satisfying the high peak luminosity and relatively cool photospheric temperature.

6.3. *Asphericity*

In all of the preceding discussion, we have necessarily assumed spherical symmetry in order to convert our observations into intrinsic quantities. However, core-collapse SNe are all known to be aspherical at some level (e.g., Wang & Wheeler 2008). The most basic effect of asphericity is to increase the uncertainty in $L_{\rm bol}$ and dilute the connection between observables such as the rise time and physical quantities such as the diffusion timescale.

The broad-lined SNe Ic associated with GRBs have been extensively studied in the context of aspherical models, with different studies coming to conflicting conclusions for the same object (e.g., SN 1998bw: Höflich et al. 1999; Maeda et al. 2006). The models of Maeda et al. (2006) for SN 1998bw predict that lines of sight along the major axis of a bipolar outflow will see light curves with faster rise times and higher luminosities than average, perhaps indicating a general trend with relevance for PS1-10afx. However, despite the high explosion energies ($>10^{52}$ erg) and fairly high nickel masses ($\sim$0.4 M$_\odot$) assumed in their models, the maximum peak luminosity was still an order of magnitude lower than for PS1-10afx. In addition, the spectral features of PS1-10afx are not as blended as those of broad-lined SNe Ic (Figure 6). We conclude that an aspherical SN 1998bw-like model is unlikely to produce an object that resembles PS1-10afx unless some other ingredient is added to the models.

Another possibility in a CSM interaction scenario is that the material with which the SN is interacting is distributed in an aspherical fashion, perhaps allowing a distant observer to see both the luminous continuum emission from the interaction region and the SN ejecta. However, such models still require the combination of the covering fraction of the CSM, the radiative efficiency factor, and the SN kinetic energy to be sufficiently high to produce the $\sim10^{51}$ erg of optical emission that we measure. The SLSN models of Metzger (2010) invoke remnant protostellar disks around massive stars, but do not simultaneously fit the high peak luminosity and the fast timescale of PS1-10afx. In addition, such a model has similar difficulties as spherical CSM interaction models in explaining the strength of the P-Cygni features in the observed spectra if there is continuum emission from an interaction region that dilutes the strength of the spectral features from the ejecta.

7. CONCLUSIONS

We present multiwavelength observations of PS1-10afx at redshift $z = 1.388$, perhaps the most luminous SN yet discovered. The combination of observables presents strict constraints on any theoretical interpretation. These are:

- A peak bolometric luminosity of 4.1×10^{44} erg s^{-1}
- An observed rise time of $\sim$12 d
- A fast light curve decay, with Δm_{15}= 0.95 mag
- At least 7×10^{50} erg of optical radiation emitted, with a total likely closer to 10^{51} erg
- Red color near maximum light ($T_{\rm BB}$ = 6800 K), although $T_{\rm eff}$ may be closer to 12,000 K
- Constant UV color before maximum light
- Photospheric velocities near maximum light of $\sim$11,000 km s^{-1}
- Spectra that most closely resemble normal SNe Ic, with deep Ca II P-Cygni absorption
- Photometric and spectroscopic evidence for some line blanketing in the NUV from iron-peak elements, although not as much as for SNe Ia
- A massive ($\sim2\times10^{10}$ M$_\odot$) host galaxy that is unlikely to have an extremely low metallicity

We surveyed existing models for SLSNe and found that none were acceptable. In particular, the large inferred $R_{\rm BB}$ near maximum light is very hard to reconcile with the fast observed rise time and the measured photospheric velocities because the SN ejecta need too much time to reach such large radii. The magnetar models that match the peak luminosity and rise time do so by producing a much higher temperature at a smaller radius. These flaws are generic to models powered by internal energy sources, although if the onset of the internal energy source can be sufficiently delayed after the initial explosion, then maybe the conflict between the velocities and radii can be avoided. Shock breakout scenarios invoking dense CSM provide a promising solution by allowing the SN to explode well before the optical emission is detectable. If the CSM is sufficiently dense out to $\sim 5\times10^{15}$ cm, then the light curve will only rise after the ejecta have had time to reach that radius. However, these models leave the normal SN Ic-like spectrum unexplained and are in apparent conflict with the observed color evolution before maximum light. More detailed radiative transfer calculations of the models are necessary to know whether these flaws can be avoided. In addition, it is not clear how to produce the special CSM structure that has to be assumed (a truncated wind or a shell).

PS1-10afx was initially identified as an object of interest due to its unusual colors ($r_{\rm P1} - i_{\rm P1} \approx 2$ mag at peak) and would not have been found without the PS1 observation strategy, which includes regular $i_{\rm P1}$ and $z_{\rm P1}$ observations as part of the search. At redshifts below $\sim$1, an object like PS1-10afx would have a strong detection in $r_{\rm P1}$ and would not stand out without knowing the redshift. Unlike many of the SN 2005ap-like SNe, the time-dilated light curve of a PS1-10afx-like SN at lower redshift would not be unusually long and would not be associated with the attention-grabbing lack of a visible host galaxy. However, PS1-10afx was more than a magnitude brighter than its host galaxy, which potentially provides a selection criterion to increase the odds of finding similar objects in the future. In the sample of SLSNe found by PS1, SN 2005ap-like objects (Chomiuk et al. 2011; Berger et al. 2012; Lunnan et al. 2013) outnumber PS1-10afx by at least an order of magnitude. Our poor understanding of spectroscopic incompleteness and the relevant selection effects precludes a more precise estimate of rates at this time.

An additional complication to be considered is the role of metallicity. The massive host of PS1-10afx is in contrast with the low-mass (Neill et al. 2011) and low-metallicity (Young et al. 2010; Chen et al. 2013; Lunnan et al. 2013) hosts of known hydrogen-poor SLSNe. The natal composition of the progenitor could have an indirect effect on the explosion through stellar evolutionary processes or it could directly affect the appearance through the opacity in the outer ejecta (could SN 2005ap-like events with higher metal abundances exhibit line-blanketed spectra like PS1-10afx?).

Most of the published SLSNe that lack hydrogen in their spectra are similar to SN 2005ap and SCP06F6 (Quimby et al. 2007; Barbary et al. 2009; Quimby et al. 2011; Pastorello et al. 2010; Chomiuk et al. 2011; Leloudas et al. 2012; Lunnan et al. 2013). SN 2007bi (Gal-Yam et al. 2009; Young et al. 2010) and a couple of as-yet unpublished objects (Gal-Yam 2012) were the only known exceptions. They exhibited rather different spectra and had very slow light curve decays, which were interpreted by Gal-Yam et al. (2009) to be the result of decay of a large amount of radioactive ^{56}Ni produced in a pair-instability explosion. This result has been challenged on theoretical grounds by Dessart et al. (2012b), who show that the observations do not match theoretical expectations for pair-instability SNe. With the discovery of PS1-10afx, we now have further evidence that the most luminous SNe are a heterogeneous lot, even when just considering the objects lacking hydrogen. A key question for future investigations is whether these diverse outcomes of stellar evolution can be produced by variations on a single underlying physical model or whether multiple pathways exist to produce SNe of these extraordinary luminosities. PS1-10afx differs from existing SLSNe-I in almost every observable except for the peak luminosity. It is hard to understand how all of these differences could be produced with only small modifications to a single model, and may indicate that PS1-10afx is the first example of a different channel for producing SLSNe.

This paper includes data gathered with the 6.5-m Magellan Telescopes located at Las Campanas Observatory, Chile. We thank the staffs at PS1, Gemini, Magellan, and the VLT for their assistance with performing these observations. We are grateful for the grants of DD time at Gemini and the VLT. We acknowledge J. Strader for obtaining some FourStar observations, as well as the MMIRS observers who helped obtained some of the data here during the fall 2010 queue observations: M. Kriek, I. Labbe, J. Roll, D. Sand, and S. Wuyts. SJS acknowledges funding from the European Research Council under the European Union's Seventh Framework Programme (FP7/2007-2013)/ERC Grant agreement n$^{\rm o}$ 291222. The Pan-STARRS1 Surveys (PS1) have been made possible through contributions of the Institute for Astronomy, the University of Hawaii, the Pan-STARRS Project Office, the Max-Planck Society and its participating institutes, the Max Planck Institute for Astronomy, Heidelberg and the Max Planck Institute for Extraterrestrial Physics, Garching, The Johns Hopkins University, Durham University, the University of Edinburgh, Queen's University Belfast, the Harvard-Smithsonian Center for Astrophysics, the Las Cumbres Observatory Global Telescope Network Incorporated, the National Central University of Taiwan, the Space Telescope Science Institute, and the National Aeronautics and Space Administration under Grant No. NNX08AR22G issued through the Planetary Science Division of the NASA Science Mission Directorate. Some observations were obtained under Program IDs GN-2010B-Q-5 (PI: Berger), GS-2010B-Q-4 (PI: Berger), and GN-2010B-DD-2 (PI: Chornock) at the Gemini Observatory, which is operated by the Association of Universities for Research in Astronomy, Inc., under a cooperative agreement with the NSF on behalf of the Gemini partnership: the National Science Foundation (United States), the Science and Technology Facilities Council (United Kingdom), the National Research Council (Canada), CONICYT (Chile), the Australian Research Council (Australia), Ministério da Ciência, Tecnologia e Inovação

(Brazil) and Ministerio de Ciencia, Tecnología e Innovación Productiva (Argentina). Some observations were collected at the European Organisation for Astronomical Research in the Southern Hemisphere, Chile under DDT programme 286.D-5005 (PI : Smartt). The National Radio Astronomy Observatory is a facility of the National Science Foundation operated under cooperative agreement by Associated Universities, Inc. Some of the archival data presented in this paper were taken under programs GO-5623 and GO-9114 (PI: Kirshner) and were obtained from the Mikulski Archive for Space Telescopes (MAST). STScI is operated by the Association of Universities for Research in Astronomy, Inc., under NASA contract NAS5-26555. Some of the computations in this paper were run on the Odyssey cluster supported by the FAS Science Division Research Computing Group at Harvard University.

Facilities: PS1 (GPC1), Magellan:Baade (IMACS, FIRE, FourStar), Magellan:Clay (LDSS3,MMIRS), Gemini:Gillett (GMOS-N,NIRI), Gemini:South (GMOS-S), EVLA, VLT:Yepun (HAWK-I)

REFERENCES

Ahn, C. P., Alexandroff, R., Allende Prieto, C., et al. 2012, ApJS, 203, 21
Alard, C., & Lupton, R. H. 1998, ApJ, 503, 325
Arnett, W. D. 1982, ApJ, 253, 785
Barbary, K., Dawson, K. S., Tokita, K., et al. 2009, ApJ, 690, 1358
Barkat, Z., Rakavy, G., & Sack, N. 1967, Physical Review Letters, 18, 379
Berger, E., Chornock, R., Lunnan, R., et al. 2012, ApJ, 755, L29
Branch, D., Benetti, S., Kasen, D., et al. 2002, ApJ, 566, 1005
Branch, D., Jeffery, D. J., Blaylock, M., & Hatano, K. 2000, PASP, 112, 217
Cardelli, J. A., Clayton, G. C., & Mathis, J. S. 1989, ApJ, 345, 245
Chatzopoulos, E., Wheeler, J. C., & Vinko, J. 2012, ApJ, 746, 121
Chatzopoulos, E., Wheeler, J. C., Vinko, J., et al. 2011, ApJ, 729, 143
Chen, T.-W., Smartt, S. J., Bresolin, F., et al. 2013, ApJ, 763, L28
Chevalier, R. A. 2012, ApJ, 752, L2
Chevalier, R. A., & Irwin, C. M. 2011, ApJ, 729, L6
Chomiuk, L., Chornock, R., Soderberg, A. M., et al. 2011, ApJ, 743, 114
Chugai, N. N. 2001, MNRAS, 326, 1448
Dessart, L., Hillier, D. J., Waldman, R., Livne, E., & Blondin, S. 2012, MNRAS, 426, L76
Dessart, L., Waldman, R., Livne, E., Hillier, D. J., & Blondin, S. 2012, MNRAS, 244
Dexter, J., & Kasen, D. 2012, arXiv:1210.7240
Drake, A. J., Djorgovski, S. G., Mahabal, A., et al. 2011, ApJ, 735, 106
Drake, A. J., Djorgovski, S. G., Prieto, J. L., et al. 2010, ApJ, 718, L127
Dressler, A., Hare, T., Bigelow, B. C., & Osip, D. J. 2006, Proc. SPIE, 6269,
Drout, M. R., Soderberg, A. M., Gal-Yam, A., et al. 2011, ApJ, 741, 97
Erb, D. K., Quider, A. M., Henry, A. L., & Martin, C. L. 2012, ApJ, 759, 26
Faber, S. M., Willmer, C. N. A., Wolf, C., et al. 2007, ApJ, 665, 265
Filippenko, A. V. 1982, PASP, 94, 715
Foley, R. J. 2013, MNRAS, submitted, arXiv:1212.6261
Foley, R. J., Kromer, M., Marion, G., et al. 2012, ApJ, 753, L5
Foley, R. J., Papenkova, M. S., Swift, B. J., et al. 2003, PASP, 115, 1220
Fransson, C., Challis, P. M., Chevalier, R. A., et al. 2005, ApJ, 622, 991
Fynbo, J. P. U., Jakobsson, P., Prochaska, J. X., et al. 2009, ApJS, 185, 526
Gabasch, A., Bender, R., Seitz, S., et al. 2004, A&A, 421, 41
Gal-Yam, A. 2012, Science, 337, 927
Gal-Yam, A., Mazzali, P., Ofek, E. O., et al. 2009, Nature, 462, 624
Galama, T. J., Vreeswijk, P. M., van Paradijs, J., et al. 1998, Nature, 395, 670
Gezari, S., Halpern, J. P., Grupe, D., et al. 2009, ApJ, 690, 1313
Ginzburg, S., & Balberg, S. 2012, ApJ, 757, 178
Greisen, E. W. 2003, Information Handling in Astronomy - Historical Vistas, 285, 109
Hatano, K., Branch, D., Fisher, A., Millard, J., & Baron, E. 1999, ApJS, 121, 233
Hjorth, J., Malesani, D., Jakobsson, P., et al. 2012, ApJ, 756, 187
Hodapp, K. W., Jensen, J. B., Irwin, E. M., et al. 2003, PASP, 115, 1388
Hodapp, K. W., Siegmund, W. A., Kaiser, N., Chambers, K. C., Laux, U., Morgan, J., & Mannery, E. 2004, Proc. SPIE, 5489, 667
Höflich, P., Wheeler, J. C., & Wang, L. 1999, ApJ, 521, 179
Hook, I. M., Jørgensen, I., Allington-Smith, J. R., et al. 2004, PASP, 116, 425
Iwamoto, K., Nomoto, K., Höflich, P., et al. 1994, ApJ, 437, L115
Jeffery, D. J., Kirshner, R. P., Challis, P. M., et al. 1994, ApJ, 421, L27
Kaiser, N., et al. 2010, Proc. SPIE, 7733, 12K
Kajisawa, M., Ichikawa, T., Yamada, T., et al. 2010, ApJ, 723, 129
Kasen, D., & Bildsten, L. 2010, ApJ, 717, 245
Kennicutt, R. C., Jr. 1998, ARA&A, 36, 189
Kirshner, R. P., Jeffery, D. J., Leibundgut, B., et al. 1993, ApJ, 415, 589
Kissler-Patig, M., Pirard, J.-F., Casali, M., et al. 2008, A&A, 491, 941
Komatsu, E., Smith, K. M., Dunkley, J., et al. 2011, ApJS, 192, 18
Leloudas, G., Chatzopoulos, E., Dilday, B., et al. 2012, A&A, 541, A129
Lunnan, R., Chornock, R., Berger, E., et al. 2013, in prep.
McLeod, B., Fabricant, D., Nystrom, G., et al. 2012, PASP, 124, 1318
Maeda, K., Mazzali, P. A., & Nomoto, K. 2006, ApJ, 645, 1331
Maeda, K., Tanaka, M., Nomoto, K., et al. 2007, ApJ, 666, 1069
Magnier, E. 2006, Proceedings of The Advanced Maui Optical and Space Surveillance Technologies Conference, Ed.: S. Ryan, The Maui Economic Development Board, p.E5
Maguire, K., Sullivan, M., Ellis, R. S., et al. 2012, MNRAS, 426, 2359
Mannucci, F., Cresci, G., Maiolino, R., Marconi, A., & Gnerucci, A. 2010, MNRAS, 408, 2115
Maraston, C. 2005, MNRAS, 362, 799
Mazzali, P. A., Deng, J., Maeda, K., et al. 2002, ApJ, 572, L61
Metzger, B. D. 2010, MNRAS, 409, 284
Millard, J., Branch, D., Baron, E., et al. 1999, ApJ, 527, 746
Miller, A. A., Chornock, R., Perley, D. A., et al. 2009, ApJ, 690, 1303
Moriya, T. J., & Maeda, K. 2012, ApJ, 756, L22
Moriya, T. J., & Tominaga, N. 2012, ApJ, 747, 118
Moriya, T. J., Blinnikov, S. I., Tominaga, N., et al. 2013, MNRAS, 428, 1020
Nakar, E., & Sari, R. 2010, ApJ, 725, 904
Neill, J. D., Sullivan, M., Gal-Yam, A., et al. 2011, ApJ, 727, 15
Nomoto, K., Suzuki, T., Shigeyama, T., et al. 1993, Nature, 364, 507
Nugent, P. E., Sullivan, M., Cenko, S. B., et al. 2011, Nature, 480, 344
Ofek, E. O., Cameron, P. B., Kasliwal, M. M., et al. 2007, ApJ, 659, L13
Ofek, E. O., Rabinak, I., Neill, J. D., et al. 2010, ApJ, 724, 1396
Pastorello, A., Smartt, S. J., Botticella, M. T., et al. 2010, ApJ, 724, L16
Perley, D. A., Levan, A. J., Tanvir, N. R., et al. 2013, ApJ, submitted, arXiv:1301.5903
Perley, R. A., Chandler, C. J., Butler, B. J., & Wrobel, J. M. 2011, ApJ, 739, L1
Persson, S. E., Barkhouser, R., Birk, C., et al. 2008, Proc. SPIE, 7014, 95P
Podsiadlowski, P., Hsu, J. J. L., Joss, P. C., & Ross, R. R. 1993, Nature, 364, 509
Quataert, E., & Shiode, J. 2012, MNRAS, 423, L92
Quimby, R. M., Aldering, G., Wheeler, J. C., et al. 2007, ApJ, 668, L99
Quimby, R. M., Kulkarni, S. R., Kasliwal, M. M., et al. 2011, Nature, 474, 487
Rakavy, G., & Shaviv, G. 1967, ApJ, 148, 803
Rest, A., Foley, R. J., Gezari, S., et al. 2011, ApJ, 729, 88
Rest, A., Stubbs, C., Becker, A. C., et al. 2005, ApJ, 634, 1103
Richmond, M. W., Treffers, R. R., Filippenko, A. V., et al. 1994, AJ, 107, 1022
Richmond, M. W., van Dyk, S. D., Ho, W., et al. 1996, AJ, 111, 327
Riess, A. G., Macri, L., Casertano, S., et al. 2011, ApJ, 730, 119

Riess, A. G., Strolger, L.-G., Casertano, S., et al. 2007, ApJ, 659, 98
Sauer, D. N., Mazzali, P. A., Blondin, S., et al. 2008, MNRAS, 391, 1605
Sauer, D. N., Mazzali, P. A., Deng, J., et al. 2006, MNRAS, 369, 1939
Schechter, P. 1976, ApJ, 203, 297
Schlafly, E. F., & Finkbeiner, D. P. 2011, ApJ, 737, 103
Schlegel, D. J., Finkbeiner, D. P., & Davis, M. 1998, ApJ, 500, 525
Simcoe, R. A., et al. 2008, Proc. SPIE, 7014, 27
Smith, N., Chornock, R., Li, W., et al. 2008, ApJ, 686, 467
Smith, N., Chornock, R., Silverman, J. M., Filippenko, A. V., & Foley, R. J. 2010, ApJ, 709, 856
Smith, N., Li, W., Foley, R. J., et al. 2007, ApJ, 666, 1116
Smith, N., & McCray, R. 2007, ApJ, 671, L17
Stanek, K. Z., Gnedin, O. Y., Beacom, J. F., et al. 2006, Acta Astronomica, 56, 333
Stritzinger, M., Mazzali, P. A., Sollerman, J., & Benetti, S. 2006, A&A, 460, 793
Stubbs, C. W., Doherty, P., Cramer, C., Narayan, G., Brown, Y. J., Lykke, K. R., Woodward, J. T., & Tonry, J. L. 2010, ApJS, 191, 376
Thomas, R. C., Nugent, P. E., & Meza, J. C. 2011, PASP, 123, 237
Tonry, J., & Onaka, P. 2009, Advanced Maui Optical and Space Surveillance Technologies Conference, Proceedings of the Advanced Maui Optical and Space Surveillance Technologies Conference, Ed.: S. Ryan, p.E40.
Tonry, J. L., Stubbs, C. W., Lykke, K. R., et al. 2012, ApJ, 750, 99
Vacca, W. D., Cushing, M. C., & Rayner, J. T. 2003, PASP, 115, 389
Valenti, S., Benetti, S., Cappellaro, E., et al. 2008, MNRAS, 383, 1485
Wang, L., & Wheeler, J. C. 2008, ARA&A, 46, 433
Wheeler, J. C., Harkness, R. P., Clocchiatti, A., et al. 1994, ApJ, 436, L135
Woosley, S. E. 2010, ApJ, 719, L204
Woosley, S. E., Blinnikov, S., & Heger, A. 2007, Nature, 450, 390
Woosley, S. E., Eastman, R. G., Weaver, T. A., & Pinto, P. A. 1994, ApJ, 429, 300
Young, D. R., Smartt, S. J., Valenti, S., et al. 2010, A&A, 512, A70